Research Article www.acsami.org

Breaking Barriers in Glioblastoma Targeting through Advanced Nanoparticle Cell Membrane Coating

Daniel Jiménez-Boland, Ana Robles-Fernández, Antonio Martín-Rodríguez, Miguel Ángel Cuadros, José Ángel Traverso, Paola Sánchez-Moreno, and Mattia Bramini*,



Cite This: https://doi.org/10.1021/acsami.5c07306



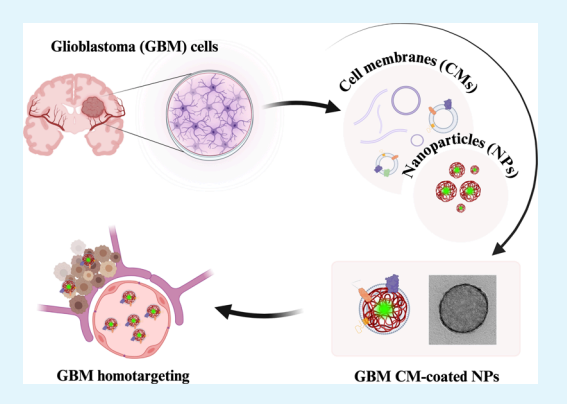
ACCESS I

III Metrics & More

Article Recommendations

Supporting Information

ABSTRACT: Glioblastoma multiforme (GBM) is the most common and aggressive malignant brain tumor characterized by poor prognosis and limited treatment options. Despite current therapies combining surgery, radiotherapy, and chemotherapy, GBM remains highly resistant to treatment, largely due to the challenges of drug delivery across the blood-brain barrier (BBB). Nanoparticles (NPs) have shown promise as drug carriers, but their clinical translation is hindered by limited brain accumulation and rapid clearance by the immune system. In this study, we explored the potential of GBM cell membrane (CM)-coated NPs (G-NPs) as a strategy to improve GBM targeting and, therefore, efficient treatments. We optimized the CM isolation protocol using U87-MG human GBM cells and identified the Heidolph homogenizer as the most effective technique for producing pure, enriched CM fractions, proposing it as a standard method due to its high scalability. G-NPs were extensively characterized, demonstrating excellent colloidal stability under



biological conditions. Flow cytometry revealed the enhanced uptake of G-NPs by U87-MG cells compared to non-coated NPs. Notably, the specific homotargeting capability of G-NPs toward human glioblastoma cells was ultimately confirmed by demonstrating a marked specificity of the glioblastoma CM coating when compared to human fibroblast CM-coated NPs, highlighting selective tumor cell-type targeting. Additionally, the coating of NPs with GBM CMs not only did not impede the physiological passage of NPs across the human in vitro BBB, but interestingly, increased the BBB permeability to G-NPs. These findings highlight that biomimetic coating of NPs with GBM cells is a potential strategy to create platforms for the targeted chemotherapy of GBM.

KEYWORDS: glioblastoma, nanoparticles, coating, cell membrane, blood-brain barrier

1. INTRODUCTION

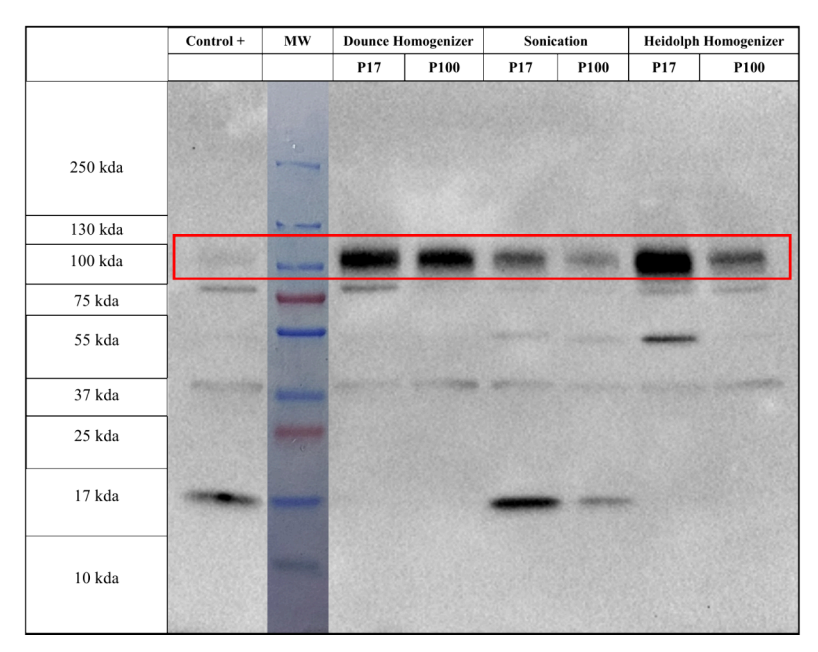
Glioblastoma multiforme (GBM) originates from uncontrolled cell proliferation of astrocytes, oligodendrocyte precursor cells, or neural stem cells in the CNS. Among all kinds of central nervous system (CNS) tumors, GBM is the most common, aggressive, and devastating malignant brain cancer.2 Traditional treatment of GBM is based on surgery to remove the neoplasm. Nonetheless, since GBM can originate or spread to several parts of the brain, surgery is not always feasible, and even when it is, the complete removal of the tumor mass is impossible in the great majority of patients.³ For these reasons, surgery events are commonly combined with radiotherapy and chemotherapy. As for chemotherapy, drugs are frequently targeted to prevent DNA replication of cells and tumor angiogenesis, such as in the case of Temozolomide (TMZ, the most common drug used against GBM). Several new chemicals have recently emerged for the treatment of GBM; nevertheless, they have only been able to delay the cancer progression without improving the survival of patients.⁴ One of the main limitations of low in vivo chemotherapeutic clinical efficiency is

the little accumulation of therapeutic agents within the nervous parenchyma because of the existence of the blood-brain barrier (BBB), composed of endothelial cells, pericytes, and astrocyte end-feet. In fact, BBB prevents hydrophilic and lipophilic molecules with a molecular weight greater than 400 Da from passing through it. Thus, BBB plays a crucial role in GBM treatment and resistance, as only around 20% of administered Temozolomide (TMZ, the most frequent drug used in GBM chemotherapy) is able to pass from the blood to the brain through the BBB. Therefore, developing new strategies to enhance drug delivery across the BBB for effective GBM treatment remains challenging.6

Received: April 11, 2025 Revised: May 12, 2025 Accepted: May 12, 2025



(a) (b)



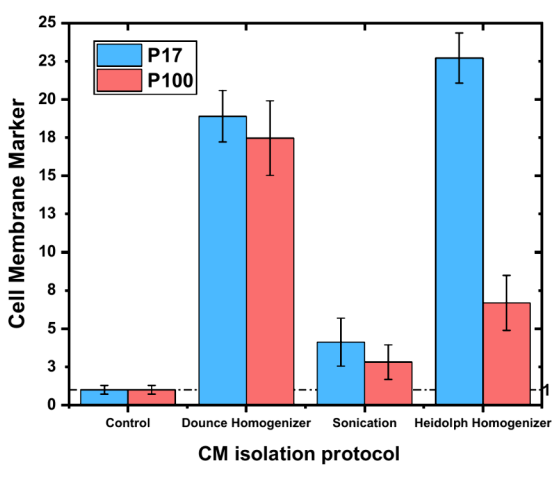


Figure 1. Cell membrane isolation protocols. (a) Western Blotting of CM P17 and P100 fractions obtained from the different CM isolation protocols. The molecular weight marker (MW) is shown as well as the control sample (total cell lysate before centrifugation). The 100 kDa band (within the red square) indicates the cell membrane marker (Anti-Na⁺/K⁺ ATPase antibody), the 75 kDa band shows the endoplasmic reticulum marker (Anti-GRP78 antibody), the 55 kDa band shows the mitochondrial membrane marker (Anti-ATP5a antibody), the 37 kDa band shows the cytosolic marker (Anti-GAPDH antibody), and the 17 kDa band shows the nucleus marker (Anti-Histone H3 (dimethyl K9) antibody). (b) Quantitative measurement of 100 kDa bands (cell membranes, highlighted in a) from different CM isolation protocols represented as the mean values of 3 different experiments ± SEM. The control density value was normalized to 1.

In recent years, nanomaterials have emerged as tools of great interest for drug delivery to the brain, both as free-nanoparticle (NP) solutions able to cross the BBB as well as locoregional nanobased implants for controlled drug release. 7-9 However, no NP formulation has so far been able to reach a relevant therapeutic brain delivery of drugs, and CNS low-dose release implants still need invasive surgery procedures. 10 As of today, two main strategies have been employed to enhance NP passage across the BBB: (i) BBB permeability modulation by ultrasound, phototherapy, radiation, and electromagnetic fields (associated with the risk of compromising the BBB integrity leading to considerable side effects), and (ii) NP surface engineering and functionalization with biomolecules or surfactants that could facilitate transcytosis through the BBB. 11-13 Some recent examples include liposomes decorated with β -amyloid (A β) peptides (A β 25–35)¹⁴ , and the functionalization of NPs with transferrin^{15,16} or ApoE.¹⁷ Although these strategies showed a small enhancement in BBB crossing, the specificity against GBM is still low, mainly due to the absence of a targeted specific GBM molecule. Moreover, the heterogeneity of CM proteins of tumor cells varies among patients, making the translation of these therapies into clinical practice difficult. Additionally, when NPs come into contact with the bloodstream, the different proteins, lipids, and carbohydrates bind onto their surface forming the biomolecular corona (BC), which, through opsonins, can activate the mononuclear phagocytic system (MPS) triggering NP early clearance. 18 The BC could also mask the surface functionalization of NPs, modifying their ability to overcome the BBB and target the tumor. 18 To address these challenges, over the past decade, cell membrane (CM)-coating nanotechnology has gained attention as an innovative strategy in

nanomedicine for creating stealth NPs¹⁹ and different cell lines have been investigated, such as red blood cells, immune cells, and cancer cells, as CM sources for coating.²⁰ The CM-coated NP preserves the original proteins, lipids, and carbohydrates from the source cell, which improves its ability to interact with biological environments. In particular, tumor-derived CMcoated NPs inherit the complex and heterogeneous surface of the original cancer CM, and the biomimetic layer offers several advantages to the NPs²¹ such as improvement of their half-life time by escaping the MPS, increased stability, and targeted delivery also known as homotargeting. Cancer CM-coated NPs have been proven to target the tumor by homologous selfrecognition mechanism between their biomimetic CM layer and the CM of the tumor cells enhancing the efficacy of drug delivery and improving therapeutic outcomes.²¹ This homotypic targeting could potentially reduce off-target effects and address the challenge of interpatient variability, where the surface heterogeneity of tumor cells often limits the effectiveness of traditional therapies. Moreover, GBM cells possess the intrinsic ability to pass through the BBB, a property critical for therapeutic strategies aimed at targeting brain tumors. 22,23 Thus, by utilizing CM derived from GBM cells, NPs may incorporate specific proteins and surface molecules that participate in the translocation across the BBB, and this could help NPs penetrate the BBB, increasing the accumulation of the transported drug in the brain.

Although the use of this biointerface strategy has been investigated for coating NPs with CMs from various cell lines, its application for the targeting of GBM has been insufficiently explored, and a standardized method for membrane extraction has yet to be established, making the results not comparable. Herein, in this study, we optimized the coating of

model polystyrene NPs with CMs from a human GBM cell line (U87-MG). GBM CM-coated NPs (G-NPs) were synthesized, characterized, and tested in vitro against GBM human cells and a human in vitro BBB model. First, we optimized the CM isolation protocol by comparing three different cell disruption techniques in order to obtain the purest and most enriched GBM CM fraction. This first step is crucial for the final G-NP assembly, and there is no agreement in the literature over the best and most efficient CM isolation procedure. The resulting G-NPs were extensively characterized in terms of size, surface charge, and colloidal stability, and their interactions with serum proteins and the subsequent formation of a protein corona were evaluated. Flow cytometry studies and optical microscopy were performed to assess the bionanointeractions between G-NPs and U87-MG cells, and finally, the influence of G-NPs coating with GBM CMs on the passage through a human in vitro BBB model was evaluated.

2. RESULTS

2.1. Optimization of Cell Membrane Isolation. U87-MG CM isolation was performed by carrying out and comparing three different procedures all starting from a previously described double centrifugation protocol (Figure S1): (i) Dounce homogenizer, (ii) Heidolph homogenizer, and (iii) sonication. The first pellet (P17 fraction) was obtained by a first centrifugation at $17,000 \times g$ and the second pellet (P100 fraction) by a second centrifugation at $100,000 \times g$. The protein content of both pellets was quantified by a BCA kit (see Materials and Methods). Of note, the total protein content obtained by the BCA assay showed that the P100 fraction from Dounce homogenizer and Heidolph homogenizer protocols was lower than the P17 fraction. On the contrary, following the sonication protocol, the P100 fraction yielded a higher protein content compared to the P17 one (Table S1).

The purity and CM enrichment of both P17 and P100 fractions from each of the 3 tested protocols were then compared to determine the most suitable methodology for CM isolation. SDS-PAGE electrophoresis gel was run to identify and semiquantify the different components of both fractions. The total cell lysate before centrifugation used as the positive control (control +) was also analyzed (Figures 1a and S2a,b). Notably, all three protocols showed greater band intensity than the control +, reflecting membrane isolation by centrifugation, while the control represents cell lysis prior to this step. The first detectable band (100 kDa) was identified as the CM marker Na⁺/K⁺ ATPase; bands at 75, 55, 37, and 17 kDa were instead identified as the endoplasmic reticulum, the mitochondrial membrane, cytosol, and nucleus, respectively.

The results from the sonication procedure displays a higher number of detectable bands, both in the P17 and P100 fractions, likely indicating less pure CM content with endoplasmic reticulum (70 kDa), mitochondrial (55 kDa), and nuclear contamination (17 kDa). On the other hand, bands obtained from the Dounce and Heidolph homogenizer protocols suggested a greater purity of the isolated CM fractions (CMF). The best results in terms of purity were obtained from the P100 fraction of Dounce and Heidolph homogenizer procedures, presenting a high CM content with minimal mitochondrial and endoplasmic reticulum contamination and no detectable bands for the nucleus. A semi-quantitative analysis of P17 and P100 fraction bands was then carried out (Figure 1b). Remarkably, all three CM isolation

protocols showed higher CM enrichment than the control sample (total cell lysate before centrifugation). However, the sonication procedure displayed the smallest amount of purified CM compared to that of the Dounce and Heidolph homogenizers, suggesting that homogenization is more effective than sonication for CM purification. Although it could be thought that the samples of the sonication protocol contained a lower disrupted cellular content than the samples of the Dounce and Heidolph protocols, it is important to highlight that all the Western Blot samples were loaded at the same protein concentration, as confirmed by the Coomassie Blue-stained SDS-PAGE gel prepared simultaneously with the Western Blot (Figure S2a).

Although P17 fractions from both Heidolph and Dounce homogenizers displayed the highest CM levels (100 kDa band), they also showed significant contamination with endoplasmic reticulum and nuclei residues. Thus, we focused on the P100 fraction as the purest CMF, and, in particular, the P100 fraction obtained through a Heidolph homogenizer. In fact, the Heidolph homogenizer protocol is characterized by a higher reproducibility, since the cell disruption procedure is automated, resulting in a promising approach for future standardization of CM isolation protocols. For this reason, the P100 fraction obtained from the Heidolph homogenizer protocol was selected for subsequent NP surface coating.

2.2. Nanoparticle Surface Coating and Characterization. 2.2.1. Characterization of NP Coating. Fluorescein (FITC)-loaded carboxylate polystyrene NPs (PS-NPs) with an excitation/emission wavelength of 505/515 nm were used as model NPs to investigate the coating with isolated CM from the U87-MG cell line. Dynamic light scattering (DLS) was performed to characterize CMF P100, bare PS-NPs, and GBM CM-coated PS-NPs (G-NPs) in Milli-Q water. The measurements included hydrodynamic diameter ($D_{\rm H}$), polydispersity index (PDI), and surface charge (Z-potential). The results, shown in Table 1 and Figure 2a, indicate a higher $D_{\rm H}$ for G-

Table 1. Characterization of NP Coating^a

	size (nm)	PDI	Z-potential (mV)
CMs	190.0 ± 40.0	0.66 ± 0.11	-22.0 ± 4.0
PS-NPs	119.9 ± 1.5	0.06 ± 0.02	-45.0 ± 3.0
G-NPs	153.3 ± 6.0	0.16 ± 0.02	-26.2 ± 3.0

^aSize, PDI, and Z-potential of CMs, PS-NPs, and G-NPs. Data are represented as the mean average of 4 independent replicates ± SEM.

NPs compared to bare PS-NPs, with values of 153.3 \pm 5.5 nm and 119.9 \pm 1.5 nm, respectively. This difference in size can be attributed to the CM coating effect. In terms of Z-potential (Table 1 and Figure 2b), the G-NPs exhibited a considerably less negative charge than the PS-NPs (-26.2 ± 3.2 and -45.0± 3.3 mV, respectively), which is consistent with a successful coating process, considering the value of the Z-potential of the CM fraction alone ($-22 \pm 4.0 \text{ mV}$). The PDI (Table 1) of G-NPs is 0.16 ± 0.02 , suggesting a monodisperse colloidal system, although it is slightly higher than the PDI value of commercial PS-NPs (0.06 \pm 0.02). Due to the biological variety of sizes of the proteo-lipid patches, the D_H standard deviation of CM was far higher than that of the PS-NPs and G-NPs, as well as the PDI values. Overall, DLS results confirmed the successful coating of G-NPs, as evidenced by the increase in size and the change to a less negative surface compared to bare PS-NPs, in agreement with previous findings.²⁹ Finally, to

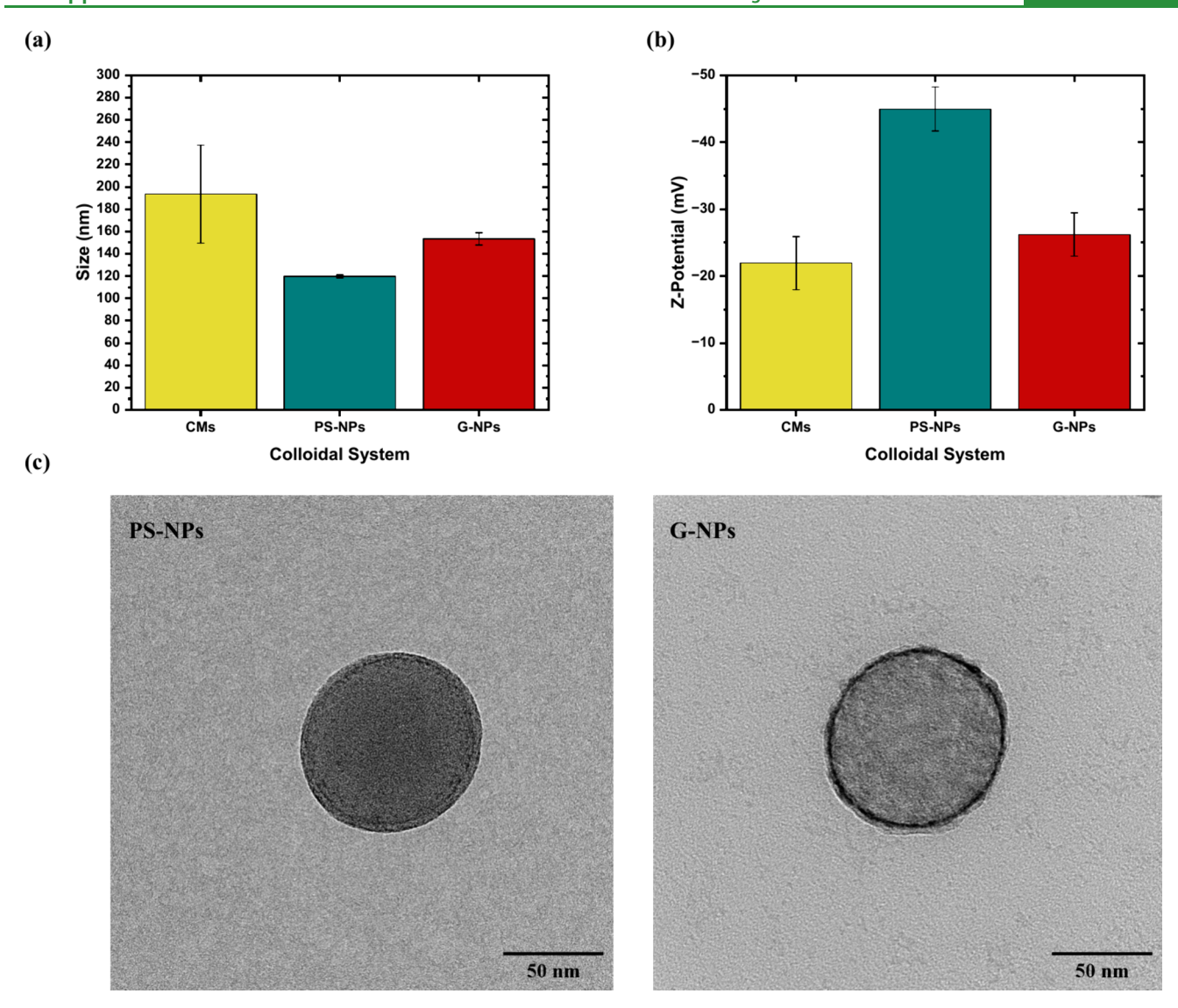


Figure 2. Characterization of NP coating. (a) Size (nm) of CMs, PS-NPs, and G-NPs by DLS in Milli-Q water at RT. (b) Z-potential (mV) values of CMs, PS-NPs, and G-NPs in water at RT. Data are represented as the mean average of 4 independent replicates ± SEM. (c) TEM micrographs of PS-NPs and G-NPs showing the CM coating layers onto the G-NPs surface.

further validate the CM coating, TEM micrographs of PS-NPs and G-NPs were acquired, and representative images are shown in Figure 2c. The successful coating is clearly visible in the G-NPs, where a thick, dense lipid layer wraps around the entire NP (Figure 2c, G-NPs).

2.2.2. Colloidal Stability. The colloidal stability of both PS-NPs and G-NPs was assessed by DLS along a pH range (from pH 4 to pH 9) by measuring D_H and Z-potential (Figure 3a,b). Detailed data, including PDI values, are provided in Table S2. The Z-potential of PS-NPs remained negative over the entire pH range. In contrast, G-NPs shifted from positive Z-potential values to negative surface charge at pH 5-6, identifying their isoelectric point (IEP) at around pH 5 (Figure 3a). Accordingly, D_H measurements (Figure 3b) revealed an increase in G-NPs size at their IEP (pH 5), presumably due to aggregation under this specific environmental condition. Nevertheless, at physiological pH (7.4), G-NPs size remained unchanged, and their colloidal stability was preserved across the pH spectrum. Additionally, as shown in Figure S3, the $D_{\rm H}$ of CMs remained stable throughout all of the pH solutions tested.

Moreover, we investigated how these systems respond within representative biological media, including PBS, serumfree culture media (SF-DMEM), and culture media completed with 10% FBS (cDMEM). PS-NPs and G-NPs were incubated with these media, and the size ($D_{\rm H}$) was measured by DLS at 24 and 72 h (Figure 3c,d). At 24 h, some aggregation occurred in the G-NPs sample in SF-DMEM and PBS, as indicated by the increase in their size ($D_{\rm H}$, Figure 3c and Table S3). This aggregation was even more pronounced at 72 h, affecting both PS-NPs and G-NPs and suggesting a time-dependent effect on the stability of these systems (Figure 3d and Table S3). This phenomenon is likely related to the ionic strength.

Measuring the size of NPs by DLS in cDMEM presents challenges due to the polydispersity introduced by proteins. To address this, we focused on the size corresponding to the peak of the NP population rather than the average size of the entire sample. Notably, both bare NPs and CM-coated NPs, which were unstable in protein-free media and PBS, exhibited stability over time in complete culture media. This finding suggests that protein adsorption onto NP surfaces reduces aggregation due to hydration forces, which arise from

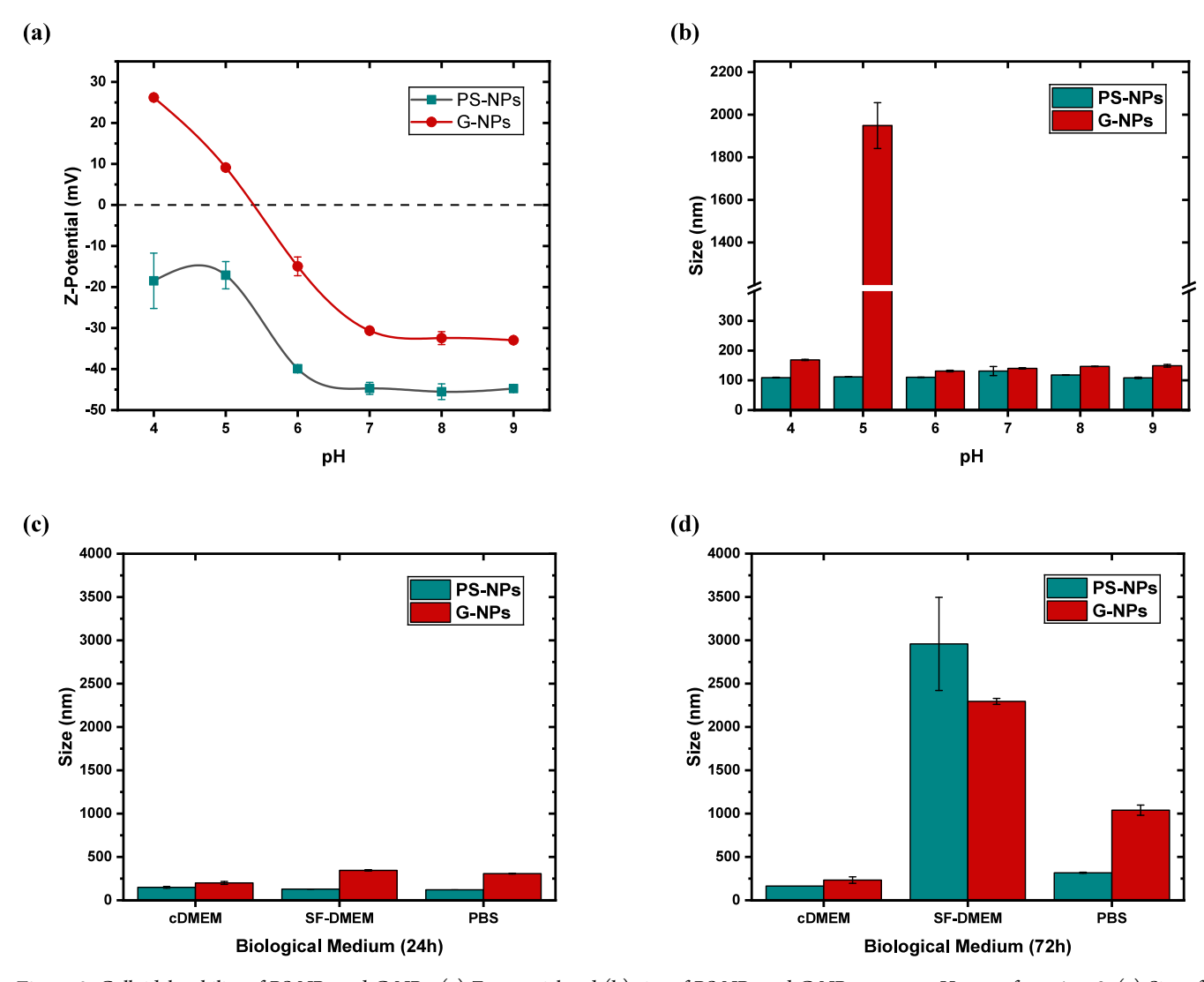


Figure 3. Colloidal stability of PS-NPs and G-NPs. (a) Z-potential and (b) size of PS-NPs and G-NPs across a pH range from 4 to 9. (c) Size of PS-NPs and G-NPs in cDMEM, SF-DMEM, and PBS after 24 and (d) 72 h of incubation. The standard deviation ± is displayed (3 replicate measurements).

interactions between the polar groups on the NPs and surrounding water molecules, forming a repulsive hydration shell. 30

The final remarks of these data prompt us to confirm the successful surface coating of G-NPs (based on the different behaviors of such a system compared to bare PS-NPs in different media and pH). Additionally, we found that G-NPs remained stable in cDMEM, the medium utilized for in vitro experiments with cells.

2.2.3. Evaluation of Biomolecular Corona Formation. The BC that forms around NPs in physiological environments critically influences their biological behavior, altering their physicochemical properties and affecting cellular interactions, uptake, distribution, and immune response. BC is typically classified into two types: the soft corona, which consists of loosely bound proteins that can exchange easily with the surrounding medium, and the hard corona, which comprises tightly bound proteins that are less likely to dissociate. Thus, BC formation onto PS-NPs and G-NPs surfaces was then evaluated. NPs were incubated with DMEM culture media supplemented with 10% FBS, and the modification of the original surface charge density due to the adsorption of

proteins was followed by Z-potential measurements. Both soft and hard coronas were evaluated along pH ranging from 4 to 9, and the results are shown in Figure 4. The Z-potential, size $(D_{\rm H})$, and PDI data obtained are summarized in Table S4.

G-NPs and NP-protein complexes exhibited behavior characteristic of proteins, with their Z-potential shifting from positive at an acidic pH to negative at higher pH levels. Regarding PS-NPs, the systems covered by either soft corona or hard corona showed similar behavior, changing from a positive to a negative surface charge at pH 5. In contrast, the control bare PS-NPs displayed negative Z-potential values throughout the entire pH range studied (Figure 4a). The size $(D_{\rm H})$ measurements of soft-corona and hard-corona of PS-NPs remained similar along the pH range, presenting a slight increase at pH 4 and 5, where the IEP was found (Figure 4b). On the contrary, bare G-NPs, as well as G-NPs with soft and hard coronas, showed a consistent trend in both Z-potential and size values along the tested pH range (Figure 4c,d). The Zpotential switched from positive to negative values at around pH 5 for all three conditions, presenting an increase in size due to the aggregation of G-NPs at pH 5. Although the binding of proteins onto the NP surface triggers a more positive charge at

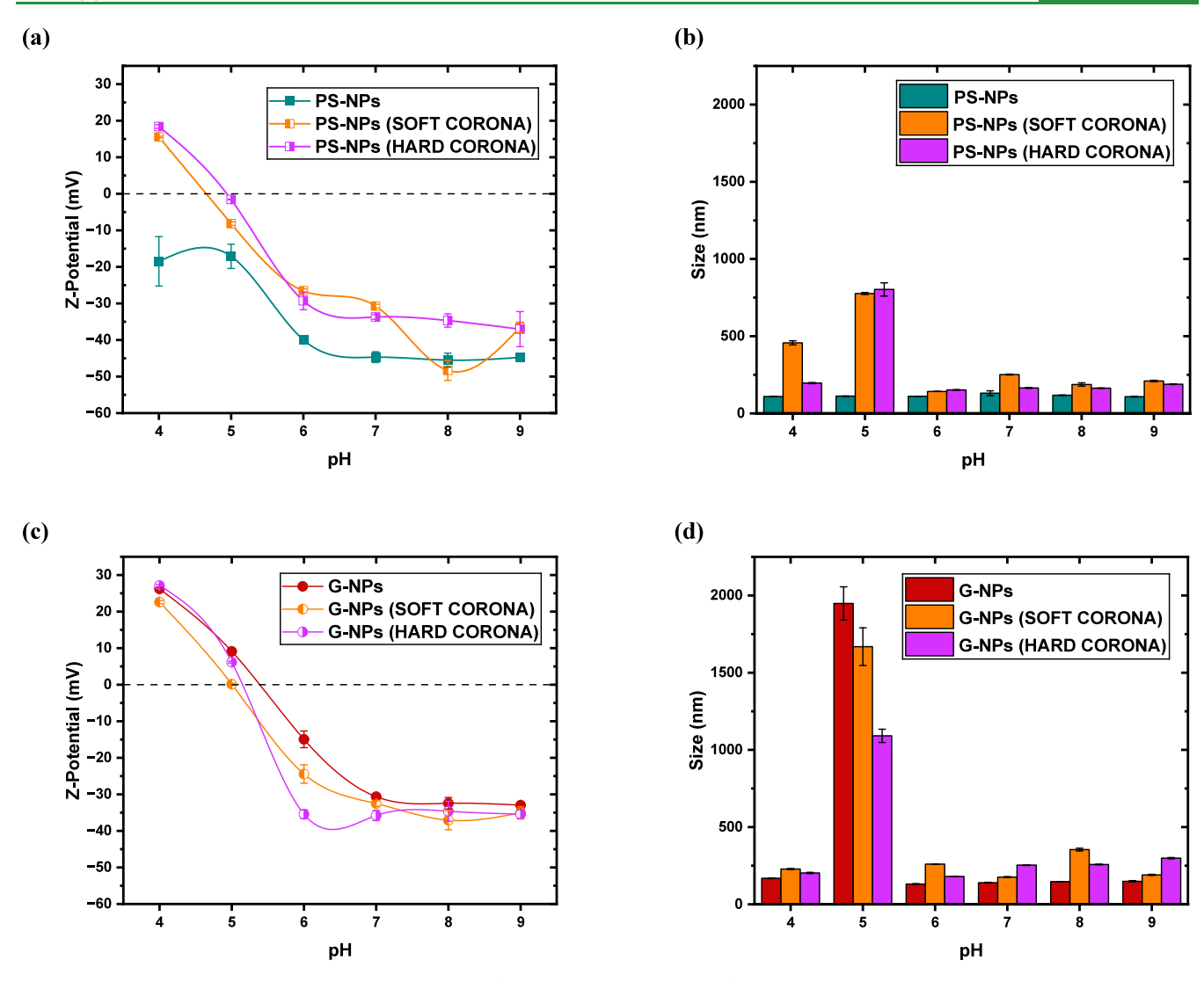
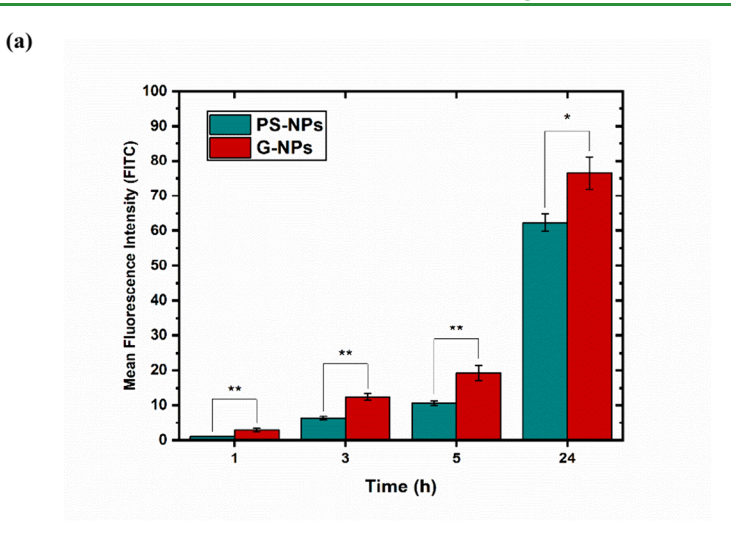


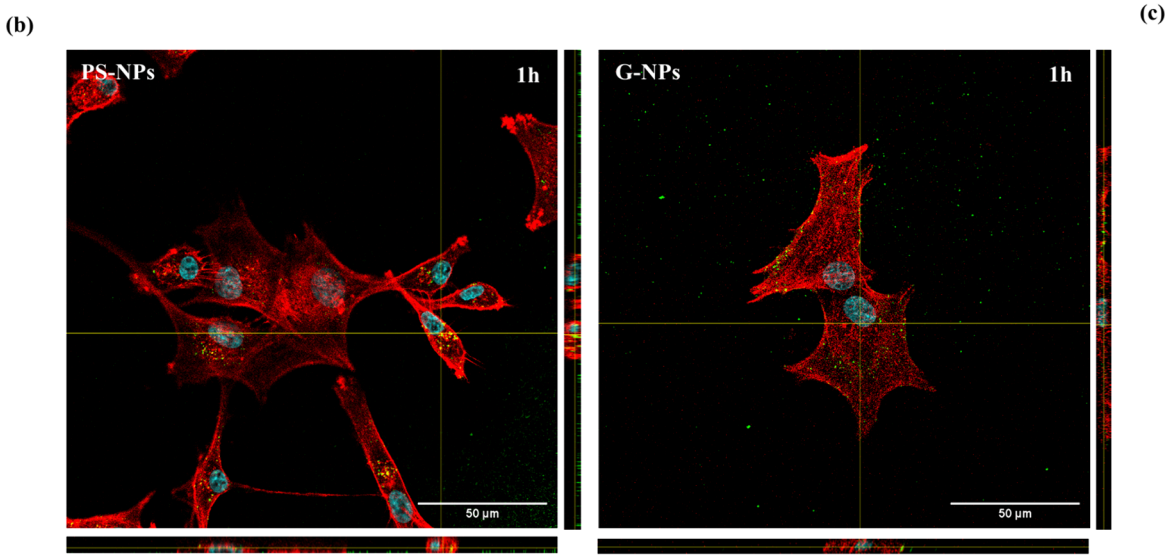
Figure 4. Assessment of biomolecular corona formation. (a) The Z-potential and the (b) size of PS-NPs are shown along a pH range, comparing bare PS-NPs, soft corona PS-NPs, and hard corona PS-NPs. (c) The Z-potential and the (d) size of G-NPs are shown along a pH range, again comparing bare PS-NPs, soft corona PS-NPs, and hard corona PS-NPs. The standard deviation is displayed (3 replicate measurements).

acidic pH, soft and hard-corona PS-NPs displayed a less positive charge compared to G-NPs and G-NPs-protein complexes. These results confirm the successful coating of G-NPs and suggest that G-NPs were able to avoid the protein corona formation event to a greater extent than PS-NPs due to the coating with CMs in agreement with previous findings.³² Moreover, the presence of either loosely bound or tightly bound proteins does not notably alter the surface charge characteristics of the NPs within this pH context. While the composition of the protein corona may differ, the overall impact on the physicochemical properties remains consistent. However, the distinction between soft and hard coronas may still be crucial in shaping biological interactions. Moving forward, proteins from the NP-protein complexes were separated by SDS-PAGE to assess differences in corona composition (Figure S4a).³³ Similar banding patterns were observed for both PS-NPs and G-NPs incubated with complete DMEM, indicating the adsorption of comparable protein species. In contrast, G-NPs coated with U87-MG cell membranes (prior to incubation with complete DMEM) displayed a distinct banding pattern compared with Ps-NPs, likely reflecting the presence of membrane-associated proteins.

Since no major differences in band intensity were observed qualitatively by SDS-PAGE, the total amount of protein in the corona was quantified using a BCA assay (Figure S4b). After subtraction of background values obtained from G-NPs not incubated with proteins (used as a control), G-NPs showed a slightly higher protein content; however, this difference was not statistically significant. It is worth highlighting that, despite no significant differences in the amount and species of proteins adsorbed onto PS-NPs and G-NPs, their biological behavior differed markedly in terms of uptake by U87-MG cells (Figure 5 and Section 2.3), underscoring the crucial and specific role of the CM coating in cell-type targeting, recognition, and uptake.

2.3. Assessment of PS-NPs and G-NPs In Vitro Targeting Abilities. To assess the *in vitro* GBM targeting abilities of G-NPs, flow cytometry was carried out to quantify the bionanointeractions between G-NPs and U87-MG cells, comparing the results with those of bare PS-NPs. Flow cytometry analysis was performed at different times (1, 3, 5, and 24 h) for both PS-NPs samples and G-NPs samples in cDMEM (Figure 5a). Since flow cytometry detection cannot distinguish between CM-adhered particles and internalized ones, we additionally performed epifluorescent microscopy





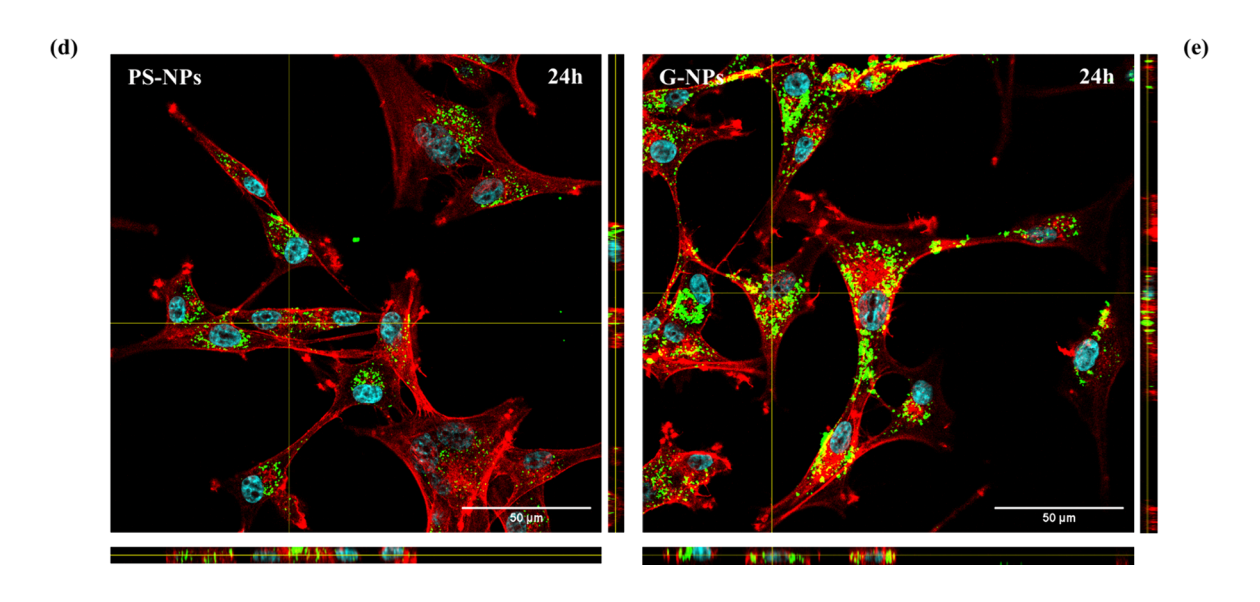


Figure 5. PS-NPs and G-NPs bionanointeractions with U87-MG cells measured by flow cytometry and confocal microscopy. (a) Flow cytometry. Statically significant differences (T-student mean comparison test p < 0.05) are highlighted with "*". The SEM is displayed (4 independent replicates). (b) (c) PS-NPs and G-NPs bionanointeractions at 1 and 24 h (d, e) and their orthogonal views (XZ and YZ) under confocal microscopy. Confocal microscopy samples were stained with Hoechst (blue nucleus), phalloidin (red cytoskeleton), and FITC- (green NPs).

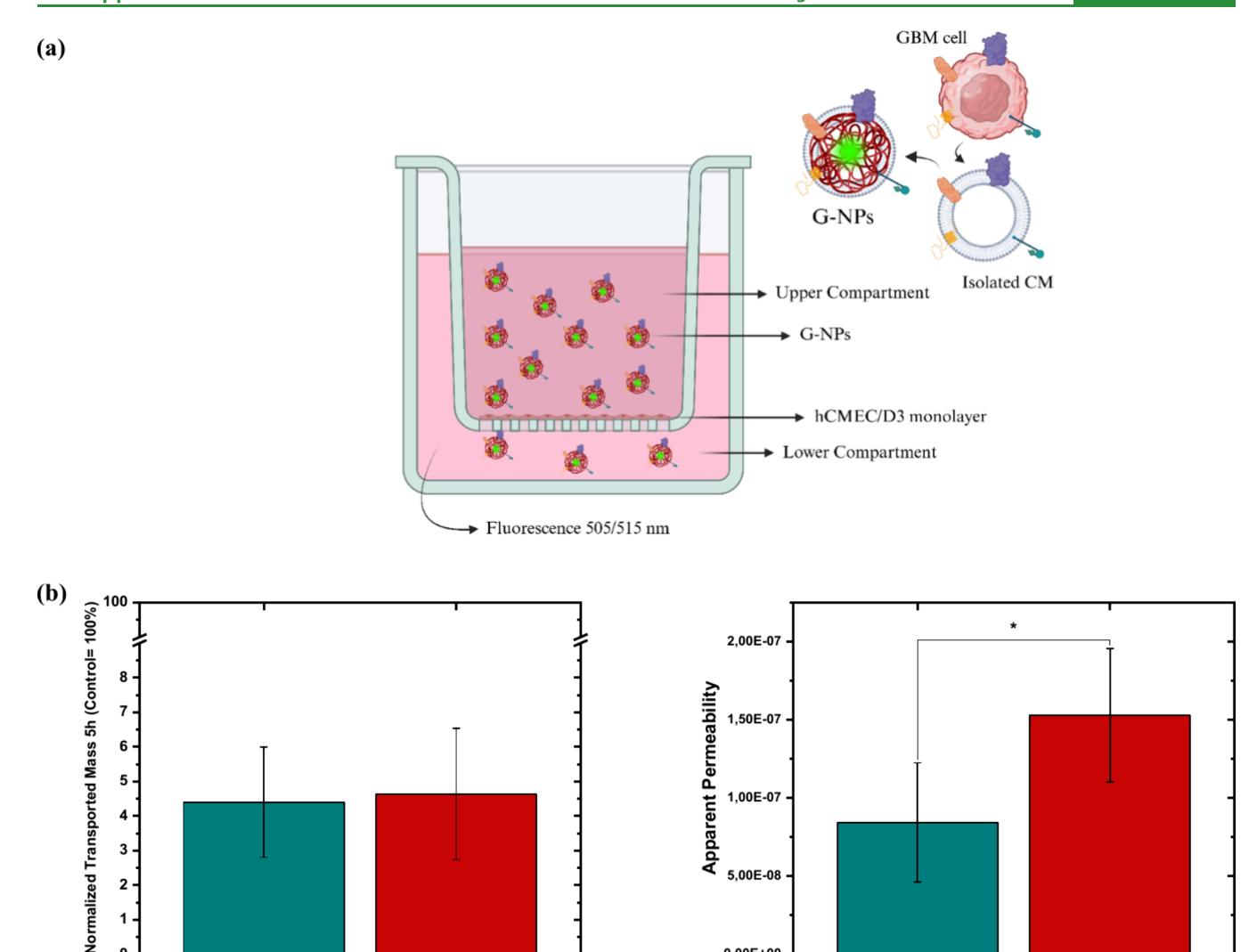


Figure 6. Transport Study of PS-NPs and G-NPs across the in vitro BBB model. (a) Schematic representation of the passing assay across the in vitro BBB model (created in BioRender.com). (b) Normalized Transported Mass and Apparent Permeability of PS-NPs and G-NPs through the in vitro BBB model at 5h. Mean ± standard deviation is displayed (9 replicate measurements). Statically significant differences (T-student mean comparison test p < 0.05) are highlighted with "*".

5,00E-08

0.00E+00

(Figure S5) and fluorescence laser scanning confocal microscopy (CLSM) to better visualize and discriminate G-NPs interactions with glioblastoma U87-MG cells (Figure 5).

PS-NPs

G-NPs

3

2

The flow cytometry experiment analyzed the mean fluorescent intensity of U87-MG cells exposed for 1, 3, 5, and 24 h to 20 μ g/mL PS-NPs and G-NPs in cDMEM, with mean fluorescence intensity data normalized to a PS-NP FITC mean fluorescence intensity of 1.00 at 1 h (Figure 5a). The results display a significant difference between PS-NPs and G-NPs at all the time points tested showing higher fluorescence for G-NPs, thus suggesting a higher interaction with GBM cells. These results were confirmed by confocal microscopy and fluorescence microscopy (Figures 5b-e and S5). The images display PS-NPs and G-NPs in green, cell nuclei in blue, and the cell cytoskeleton (phalloidin staining for actin filaments) in red. Confocal cross-sections and lateral section images show PS-NPs and G-NPs internalization in U87-MG cells, strengthening the flow cytometry data by displaying active targeting of G-NPs towards GBM cells. Furthermore, images obtained from confocal microscopy acquisition were analyzed by plotting the Z-axis profile (Figure S7; Z-axis

fluorescence analysis). The orthogonal and lateral views showed that both PS-NPs and G-NPs were localized either on the cell surface (especially at early time points, Figure 5b,c) and inside the GBM cells (at later time point, Figure 5d,e), with high accumulation in the perinuclear area. Accordingly, the Z-axis fluorescence analysis at 24 h of exposure (Figure S7) revealed that both PS-NPs and G-NPs were located more centrally on the Z-axis compared to the cell cytoskeleton, which is consistent with cell internalization and, therefore, cell uptake events.

PS-NPs

Altogether, these results reveal that G-NPs were successfully able to enhance the biointeractions with the glioblastoma U87-MG cells in vitro compared to bare PS-NPs. This effect is most probably related to self-recognition mechanisms between the U87-MG CM layer that covers the G-NPs and the surface receptors and biomolecules of GBM cells. Thus, the results proved a higher and more specific targeting and uptake of G-NPs by GBM cells. To further validate this outcome and exclude any random effect of the biological coating, NPs coated with CMs extracted from the human MRC-5 fibroblast cell line were prepared (F-NPs) and exposed to U87-MG cells

G-NPs

and MRC-5 cells (Figure S6). Both G-NPs and F-NPs were tested against the U87-MG cell line (Figure S6b). F-NPs were first characterized for their hydrodynamic diameter and Zetapotential in Milli-Q water to confirm the presence of the coating. F-NPs exhibited a $D_{\rm H}$ of 233.4 \pm 7.8 nm, a PDI of 0.381 ± 0.028 , and a Z-potential of -27 ± 1 mV. Similar to G-NPs, F-NPs showed a reduced Z-potential compared to the non-coated PS-NPs (-45.0 \pm 3.0 mV), indicating the successful incorporation of the fibroblast cell membrane coating. The results presented in Figure S6a demonstrate that F-NPs were more efficiently internalized by MRC-5 cells compared to G-NPs at all time points examined. In contrast, F-NPs showed lower uptake by U87-MG cells than G-NPs, with the exception of the 24 h time point (Figure S6b). Although the presence of a cell membrane coating enhances cellular uptake (both F-NPs and G-NPs are internalized to a greater extent than non-coated PS-NPs), our results suggest that the tissue origin of the membrane coating is crucial for specific recognition mechanisms or homotargeting.

2.4. Evaluation of PS-NPs and G-NPs Passage through an In Vitro Human Blood-Brain Barrier Model. The transport of G-NPs across a human in vitro BBB model was assessed in order to explore whether the coating of NPs with GBM CMs affects the ability of NPs to overcome this biological barrier. The transport study was performed using a transwell system where a hCMEC/D3 (a human brain microvascular cell line) monolayer was grown for 8 days. G-NPs and PS-NPs were loaded in the apical compartment at a concentration of 20 µg/mL and their accumulation in the basolateral chamber after 5 h of incubation was quantified by measuring the fluorescence intensity (as detailed in the Materials and Methods section and Figure 6a). The transendothelial electrical resistance (TEER) was also monitored before and after the G-NPs and PS-NPs exposure to evaluate the monolayer integrity and exclude NP passage due to barrier disruption. The in vitro BBB displayed good TEER values, in line with the already published ones for the same cell line,³⁴ which is consistent with the assembly of a functional and resistant brain endothelium (Figure S8). Moreover, these values remain unaltered after G-NPs and PS-NPs exposure, suggesting the very high biocompatibility of such systems.

The transport study of PS-NPs and G-NPs across the in vitro BBB model is shown in Figure 6b. The data do not show statistical differences at 5 h between PS-NPs and G-NPs crossing, which confirmed that the coating of G-NPs with GBM CMs does not prevent G-NPs from passing through the BBB, even though they are endowed with a larger size. Remarkably, a significant tendency was observed for G-NPs to show greater apparent permeability (P_{app}) compared to PS-NPs. These results take on even greater importance if we consider that the passage of PS-NPs at 5h through empty transwells (control samples) was slightly higher compared to G-NPs (49.1 \pm 13.5 and 43.7 \pm 9.9, respectively; Figure S9). In this regard, the coating of G-NPs with GBM CM shows a promising effect for BBB crossing and GBM targeting, and it does not compromise the passage of NPs. In contrast, PS-NPs cores were not able to successfully cross the in vitro BBB model as results revealed, with a passage of 4.4 \pm 1.6%, which was much smaller compared to the results obtained from control samples.

In summary, even if G-NPs were not able to significantly enhance the passage through the in vitro BBB model under physiological conditions, the successful coating of G-NPs did

ı

not impair the normal passage of PS-NPs across the in vitro BBB, and showed a trend of G-NPs toward higher permeability despite the larger size. These results confirmed that coating of G-NPs with GBM CMs is a powerful tool for GBM targeting.

3. DISCUSSION

Due to the difficulties in successful GBM treatments and drug accumulation in the brain, it is essential to employ new strategies and methods that allow the survival of patients. In this regard, biomimetic nanotools show promising results for the specific targeting and drug delivery to cancer cells. Coating with CMs has been widely studied and employed with many cell types as donors. Tumor-derived CM-coated NPs were seen to inherit cancer cells' escape immunity properties and develop an extraordinary capacity to target the tumor area through a homologous self-recognition mechanism.³⁵ Additionally, they possess specific tumor antigens, which are presented by specialized antigen-presenting cells and, consequently, trigger patients' immune response.³⁶ However, this new biomimetic approach is still being investigated for brain tumors and central nervous system pathologies, where only a few studies have been presented so far.²¹ Based on the above evidence, we explored in this work innovative G-NPs using GBM CMs to target GBM cells and overcome the BBB.

One of the limiting and key steps to fabricating successful biomimetic NPs for tumor targeting is the pureness and integrity of the isolated CM then used to cover the NP surface. Cell membrane coating nanotechnology involves three main stages: cell lysis and membrane fragmentation, membrane isolation, and NP coating. CM isolation is a delicate step in which the techniques used have a high influence on the integrity of the membrane proteins that NPs inherit.²⁸ To date, a wide variety of methods have been employed for the predisruption of cells before the CM isolation, such as homogenization, sonication, and freeze-thawing, commonly combined with the foregoing hypotonic lysis. Usually, the disruption technique is not affected by the cell source but rather by the available materials and the previous experience of the research group.³⁷ The lysate is then subjected to centrifugation at 400 to 1000 g to obtain the postnuclear supernatant (PNS) fraction, free from nuclei and cell debris. Following this, the literature describes three main different centrifugation protocols to isolate CMs from the PNS. The simplest method involves differential centrifugation of the PNS at 14,000 to 20,000 g for 20-30 min, after which the pellet (referred to here as the P17 fraction) is collected as the isolated CMs.²⁴ However, another protocol found in the literature discards this first pellet and further ultracentrifuges the supernatant at 100,000 g for 30-60 min (referred to here as the P100 fraction).³⁸ A third method is based on a centrifugation (28,000 g for 30-45 min) in a discontinuous sucrose gradient (55-40-30% w/v sucrose).39

Since no standardized protocol for CM isolation has been described, the technique used could lead to different results. In a previous study, we focused on the step of membrane isolation following cell lysis, comparing different centrifugation protocols.³² However, a comparative study of the protocols for cell membrane fragmentation was lacking.

In this scenario, our first objective was to compare and describe three different CM disruption protocols and identify the most reproducible and effective approach. Specifically, we explored Dounce (manual) and Heidolph (automated) homogenizer and sonication protocols. Then, pellets obtained

after 1 (P17 fraction) or 2 steps of centrifugation (P100 fraction) were analyzed to identify the best in terms of CM purity. The results obtained showed that the Dounce homogenizer and Heidolph homogenizer protocols were able to obtain a purer and more enriched P100 fraction than the sonication protocol, which presents P100 CM levels similar to those of the control (total cell lysate before the centrifugation procedure). Thus, sonication produces more impure CMFs than manual or automated homogenization. Nonetheless, both the Dounce and Heidolph homogenizer protocols were able to achieve not only a pure P100 fraction but also a great enrichment in CM (although, as expected, the protein content of P17 is higher due to cellular compartment contamination).

Evaluating the purity and enrichment of isolated CMs is essential for achieving an effective biomimetic coating on NP surfaces. We have demonstrated that the CM fraction obtained from P17 contains a high level of intracellular antigens, which may hinder the ability of the NP to evade the immune system. In contrast, the P100 fraction produced by using the automated Heidolph homogenizer has proven to be the optimal choice for establishing standardized CM isolation protocols. This technique was chosen for NP coating due to its purity and reproducibility compared to manual Dounce homogenization.

After successful GBM U87-MG CM isolation, G-NPs were assembled, and the coating was confirmed by TEM and DLS. From the data obtained, we can speculate that the orientation of the CM onto the G-NPs is likely physiologically correct. Indeed, the negative surface charge values of G-NPs are very similar to those of CMs and significantly less negative than those of the PS-NPs. Moreover, it has been proved that surface coating of negatively charged NPs with negatively charged CMs (as in our case) is far more successful than coating positively charged NPs. This can be explained by the presence of negatively charged sialic acid moieties in the outer side of the CMs that lead the negatively charged PS-NPs to perform electrostatic interactions with the intracellular side of the CMs, presumably generating the right orientation of the CMs onto the finally assembled G-NPs. 1

The colloidal stability of the G-NPs is a critical parameter. If the system exhibits low stability, it could compromise the evaluation of its targeting ability, passage across the BBB, and potential applications in vivo. If G-NPs aggregate, their behavior changes, impairing their interaction with the cell surface, their cellular uptake, and, ultimately, their ability to escape from the mononuclear phagocytic system, triggering their early clearance from the bloodstream. G-NPs synthesized here were seen to be extremely stable in the pH range 6 to 9, which includes the important physiological pH of 7.4. This behavior is typical of negatively charged nanosystems that, due to the repulsion forces actuating, do not aggregate. 42 However, if the surface charge tends to a neutral value, then the attraction strengths take place, triggering NPs aggregation. Indeed, G-NPs reached their IEP at pH 5 and experienced an increase in size due to aggregation. The higher change in G-NP surface charge, compared with control PS-NPs, along the pH range can be explained by the different protonation states of the CM proteins covering the G-NP surface. At acidic pH, proteins are protonated, and G-NP Z-potential is positive. On the contrary, proteins are not protonated at basic pH, turning the G-NP surface charge negative. These results are also relevant in terms of biocompatibility and cytotoxicity of the G-NPs since their negative surface charge was proved to be not

toxic to cells in the uptake and transport studies (Figures 5, S5, and S8). 43,44 Moreover, the protonation effect can also be seen once BC formation is mimicked (Figure 4a). When NPs come in contact with biological media, they immediately absorb proteins and other biomolecules onto their surface, 45 forming a BC. The presence of such corona could modify the NP colloidal characteristics, such as active targeting, stability and, in the case of G-NPs, could mask the surface proteins of the CM layer inherited avoiding their homotypic targeting to GBM cells. Therefore, it is essential to know how our colloidal system behavior is in the presence of all these molecules, 46 not only looking for translational applications but also when carrying out in vitro experiments.

Our results demonstrated that G-NPs remain stable in cDMEM for up to 72 h, the maximum period tested. In contrast, they aggregate in SF-DMEM. The difference is due to the presence of proteins in cDMEM covering the G-NPs surface that provide a more hydrophilic layer, improving the hydration/solvation of G-NPs and stabilizing the colloidal system.⁴⁷ All biological experiments were conducted at 24 h, the point at which G-NPs were confirmed to be highly monodisperse and stable. This time frame was chosen because the pharmacokinetics of CNS-targeted NPs are generally much faster than 72.⁴⁸ Indeed, the high homotargeting ability and BBB crossing of G-NPs were demonstrated in vitro. Finally, as for the acidic microenvironment of GBM, one might think that G-NPs would aggregate upon reaching the tumor due to the observed aggregation at pH 5, but it must be considered that tumor microenvironment has a large amount of proteins that would maintain their colloidal stability. 49-51

Due to the complex biological environment that G-NPs must face, the evaluation of BC formation was also carried out, distinguishing between soft and hard corona at different pHs. The BC formation was extremely clear in the PS-NPs, which switch from a negative Z-potential along the whole pH range for free corona PS-NPs to a positive-negative surface charge for soft- and hard-corona PS-NPs, with an IEP around pH 5. These results are similar to soft and hard corona G-NPs and consistent with the binding of proteins onto the PS-NPs surface, which is similar to the NP coating event, since proteins, among other molecules, constitute the CM layers of G-NPs. On the contrary, the behavior of free-corona G-NPs was very similar to that of soft- and hard-corona G-NPs. We recently demonstrated that CM coating reduces protein adsorption compared to commonly used alternatives, such as PEGylation and chitosan coatings.⁵² Additionally, CM coating offers advantages over PEG or albumin coatings, which can trigger immune responses and inhibit interactions between NPs and cell membranes, respectively. 53,54 The ability of G-NPs to prevent BC formation is also crucial to achieving their intended purpose: active targeting through a self-recognition mechanism between the G-NP membrane layer and CM proteins on the tumor. This approach bypasses the protein heterogeneity limitations of traditional ligand-based targeting methods.55-

As a matter of fact, we proved by flow cytometry and confocal microscopy that bionanointeractions between G-NPs and U87-MG cells are enhanced, compared to those performed with PS-NPs. Flow cytometry revealed significant differences between PS-NPs and G-NPs bionanointeractions at times of 1, 3, 5, and 24 h (Figure 5a). These data are extremely relevant since it is proven the G-NP capability of quickly reaching the targeted tumor, possibly avoiding their clearance by the

mononuclear phagocytic system, their liver accumulation, and improving the treatment specificity in vivo. Moreover, in the in vitro context, where all of the above-mentioned biological barriers are not present, it is noteworthy that free G-NPs interact to a significantly greater extent with GBM cells compared to PS-NPs, suggesting a very strong biological effect of the GBM CM coating for active tumor homotargeting. Finally, the improved bionanointeraction between G-NPs and U87-MG cells was also visualized and confirmed by confocal microscopy (Figure 5b-e) and fluorescence microscopy (Figure S5). Since flow cytometry does not directly assess the cellular uptake, we explored G-NP cell internalization by imaging. Epifluorescence microscopy confirmed that a greater amount of G-NPs interacts with GBM cells compared to PS-NPs. Additionally, confocal microscopy displayed that both PS-NPs and G-NPs are internalized by GBM cells through zstack image acquisition and orthogonal views, once again showing higher accumulation for G-NPs compared to that of control bare PS-NPs. To investigate homotargeting further, NPs were coated with membranes from a non-GBM cell line using a human fibroblast cell line to extract the membranes and generate F-NPs. When exposed to fibroblasts, F-NPs exhibited specific recognition, showing higher uptake compared with both PS-NPs and G-NPs. In contrast, when the nanosystems were incubated with GBM cells, the results were reversed, with G-NPs displaying significantly greater interaction compared to those of both F-NPs and PS-NPs. In summary, the enhanced bionanointeractions observed between G-NPs and U87-MG cells confirmed that CM coating is an extremely promising approach to specifically target GBM cells. This was made possible since the U87-MG CMs were isolated through an automated protocol preserving their integrity and were correctly wrapped onto G-NP surface, reducing the BC formation and promoting G-NP homotypic targeting toward GBM cells.

Nevertheless, the GBM in vivo targeting is far more challenging, and the main obstacle to overcome to successfully deliver drugs to the brain is the BBB. G-NPs were designed in order to get over this biological barrier through the homotargeting property acquired by the CM coating. Biomimetic nanotools have been very poorly investigated so far and mostly in murine models or using CM from various neural tissues, including the endothelium of the BBB, neuron CM, or astrocyte CM. 58 In contrast, GBM-based biomimetic tools, such as the one here explored, could not only enhance homologous targeting to GBM cells but also successfully preserve the integrity of the BBB, as shown by the TEER results before and after G-NPs exposure. Therefore, G-NPs show promise as a safe tool to potentially transport drugs across the BBB in a safe way. In this first in vitro BBB-G-NPs interaction evaluation, both transport and apparent permeability of G-NPs were investigated and compared to standard control PS-NPs. Both systems were able to cross the in vitro BBB model in the first 5 h of exposure, emphasizing that the GBM CM coating of the G-NPs is not impeding or decreasing their ability to accumulate in the brain. On the contrary, apparent permeability data displayed a faster kinetics of G-NPs compared to PS-NPs in crossing the BBB model. It is relevant that the normal passage of PS-NPs through the in vitro BBB model is extremely low $(4.4 \pm 1.6\%)$, which could be acting as a real limitation to G-NP coating performance. Moreover, the polystyrene NP core of G-NPs was used only as a model to characterize and validate the coating of PS-NPs with GBM

CMs as a potential tool for the targeting of GBM. Thus, although we demonstrated that GBM CM coating improves the permeability of PS-NPs, the choice of NP core and NP dimension is crucial for the fabrication of successful biomimetic nanotools to target GBM. Future research will be focused on NP physicochemical parameter combination and CM coatings to create the best biomimetic tools for drug delivery to the brain.

4. CONCLUSIONS

G-NPs were successfully prepared by coating the NP surface with U87-MG CM (GBM cells) and extensively characterized. We first identified an extremely reproducible CM isolation protocol; we subsequently proved that G-NP colloidal stability at physiological pH 7.4 and in biological media is high. Moreover, the synthesized G-NP were able to prevent BC formation, leaving the inherited proteins of their surface available to target GBM cells and likely avoiding the in vivo early clearance of NPs. Indeed, G-NPs established improved biointeractions and accumulation in GBM cells in vitro through a homologous self-recognition mechanism. This active targeting approach is potentially essential in vivo to overcome the clearance of G-NPs by the immune system. Furthermore, homologous targeting will overcome the barrier of surface heterogeneity of GBM cells among patients and will enhance the G-NP access to the tumor site. Lastly, G-NPs showed promising results to cross the BBB, based on the data obtained by apparent permeability assays through a human in vitro BBB model. Future tests will explore the delivery of drugs loaded into G-NPs to brain tumor through the powerful homologous self-recognition mechanism against GBM. In this scenario, once the coating of NPs with GBM cells is validated, it is necessary to carry out new studies in order to assemble a G-NP core able to load the drug against GBM, looking forward to in vivo assays and to treat the most devastating tumor of the CNS. Finally, this standardized biomimetic strategy offers the added advantage of potentially enabling the development of personalized coatings derived from a patient's own tumor tissue. Such an approach could enhance homotargeting of the primary tumor while minimizing immune responses commonly associated with current antitumor therapies.

5. MATERIALS AND METHODS

5.1. Cell Culture. U87-MG human GBM cell line was obtained from the American Type Culture Collection (ATCC). It was cultured using the PAN Biotech Dulbecco's Modified Eagle's Medium (DMEM, Gibco) supplemented with 10% (v/v) fetal bovine serum (FBS, Gibco) and 1% penicillin–streptomycin solution (PS, Gibco) to avoid cell culture contamination. FBS was inactivated at 56 °C for 30 min. The cell line was incubated in an atmosphere with 5% $\rm CO_2$ and 95% humidity at 37 °C.

hCMEC/D3 human microvascular endothelial cell line from CNS was purchased from Cedarlane USA. These cells are able to form an in vitro brain endothelium that exhibits a polarized structure, contact inhibition at the confluence, and other features of the BBB as tight and adherence junctions. hCMEC/D3 was cultured in T-25 Flasks coated with a thin layer of Rat Collagen I (Cultrex Rat Collagen I lower, Sigma-Aldrich). After 1 h incubation at 37 °C, cells were seeded in supplemented EBM-2 Endothelial basal medium (Lonza) containing 5% v/v FBS, 1% PS, 1,4 μ M hydrocortisone, 5 μ g/mL ascorbic acid, 1% chemically defined lipid concentrate, HEPES, and 10 mM of human basic fibroblast growth factor (bFGF). hCMEC/D3 cells were incubated in an atmosphere with 5% CO2 and 95% humidity at 37 °C.

The human fibroblast cell line MRC-5 was cultured in Opti-MEM Reduced Serum Medium (Gibco) supplemented with 3% fetal bovine serum (FBS). Cells were maintained at 37 $^{\circ}$ C in a humidified atmosphere with 5% CO₂.

5.2. Isolation of Cell Membranes. The isolation of U87-MG CMs was carried out by a double centrifugation isolation protocol as previously described. 28 Briefly, cells were first grown in eight T-75 Flasks until complete confluence, which allowed up to 100 million GBM cells to be collected for each CM isolation. Cells were detached from the culture flask using EDTA-Trypsin solution (PAN-Biotech) at 0.05% concentration to preserve membrane protein integrity. Then, cells were recollected and washed in a PBS solution by centrifugation at 1500 rpm for 5 min. The pellet was resuspended in a hypotonic solution containing Tris-HCl, KCl, MgCl₂, sucrose, 10 µg/mL DNase, and 10 μ g/mL RNase at physiological pH 7.4. For cell disruption, three different methods were tested, all under ice-cold conditions. In the first protocol, cells were lysed using a traditional Dounce homogenizer (D9063 KIMBLE Dounce tissue grinder set 7 mL, Sigma-Aldrich). The second technique was performed by adopting Heidolph homogenizer DIAX 900 (Heidolph, Germany) at 66% power for 4 min, and last, the third method was based on a previously described sonication protocol.⁵⁹ For sonication, the power setting of the Branson SFX550 Sonifier (Branson Ultrasonics, USA) was tested at 16%, with on-and-off cycles of 0.5 s for 1 min and intervals of 30 s among three repetitions. Under these three different cell lysis techniques, the cell lysate was centrifuged at 1500 rpm for 5 min (Beckman Coulter Allegra 21R Refrigerated Centrifuge, USA). The supernatant was recovered and stored under ice-cold conditions, while the obtained pellet was additionally subjected to the same homogenization technique in order to obtain a more concentrated cell lysate supernatant. The supernatant was then stored as a total cell lysate control sample.

Subsequently, the supernatant was centrifuged at 17,000 × g for 30 min at 4 °C, and then the pellet was resuspended in 200 μ L of Milli-Q water and stored at -20 °C as the P17 fraction (P17). Then, the supernatant was recentrifuged at 100,000 × g for 60 min at 4 °C, and the pellet enriched in U87-MG CMs was resuspended in 200 μ L of Milli-Q water and stored at -20 °C as the P100 fraction (P100). Lastly, the membrane content of P17 and P100 fractions was analyzed indirectly by quantifying their protein content using a BCA Kit (Pierce BCA Protein Assay Kit, Thermo Fisher).

MRC-5 cell membranes were isolated using the same Heidolph homogenization protocol and double centrifugation procedure described above, with the final P100 fraction collected and stored as the membrane-enriched sample.

5.3. Western Blotting. Western blotting was carried out using a Membrane Fraction WB Cocktail (ab140365, Abcam), which contains several antibodies targeting proteins of different compartments of cells: Na+/K+ ATPase (CM), GRP78 (endoplasmic reticulum), ATP5a (mitochondrial membrane), GAPDH (cytosolic marker), and HISTONE H3 (nuclear marker). Furthermore, this cocktail includes an HRP-conjugated secondary antibody for chemiluminescent development. Therefore, for SDS-PAGE, a mixture of each sample and loading buffer containing bromophenol blue, sodium dodecyl sulfate (SDS), glycerol, Tris-HCl, and water was prepared. Samples were boiled for 3 min for protein denaturation, and $16 \mu g$ of each sample (protein content) as well as $6 \mu L$ of a molecular weight marker (Thermo Scientific Page-Ruler Plus Prestained Protein Ladder) were loaded into a Bio-Rad 4-20% Mini-PROTEAN® TGX Precast Protein Gels. For the running of SDS-PAGE, a constant field of 100 V for 60 min was applied by using a PowerPac HC High-Current Power Supply and a Mini-PROTEAN Tetra Vertical Electrophoresis Cell (Bio-Rad). The gel electrophoresis was transferred onto a Bio-Rad PVDF membrane (Trans-Blot Turbo Mini 0,2 μm PVDF Transfer Packs) using a Trans-Blot Turbo Transfer System (BioRad) for 30 min. The membrane was blocked in 5% milk-PBS-Tween 0.1% solution for 45 min at room temperature (RT) and incubated in primary antibody overnight at 4 °C. Then, the membrane was washed in PBS-Tween 0.1% solution and incubated with the secondary antibody for 60 min at RT. Finally, the membrane

was rewashed and developed with Immobilon® Western Chemiluminescent HRP Substrate (Millipore). Additionally, to verify that each sample was loaded on the gel at the same protein concentration (Figure S3), another SDS-PAGE sample was simultaneously prepared to be stained with Coomassie Blue and compared with the transferred gel, which was also stained to assess its successful transfer. Finally, semiquantification was performed using ImageJ software. Thereby, the gel plot lane tool was employed to obtain representative values for each band corresponding to the CM marker.

5.4. G-NPs and F-NPs Assembly. Carboxylate-modified microsphere FluoSpheres® (PS-NPs, Invitrogen) were used as the core of the CM coated-NPs. The PS-NPs were coated with the isolated U87-MG CMs, according to a previously described protocol,⁶⁰ and the resulting nanosystems were named as G-NPs. P100 CMF from U87-MG cells was diluted to a 1 mg/mL concentration in Milli-Q water (protein concentration from BCA assay). Thus, a ratio of 1:1, consisting of P100 CMF (1 mg/mL) and PS-NPs (1 mg/mL), was mixed under ice-cold conditions inside a glass jar. The mixture was then subjected to bath sonication for 3 min at a frequency of 50/60 Hz (JP Selecta 3000513). Therefore, binding between the PS-NPs and U87-MG CMs was achieved through electrostatic interactions. Subsequently, the mixture was centrifuged at 20,000×g for 40 min. The pellet containing the G-NPs was saved and resuspended in a lowionic buffer at pH 7 to achieve a concentration of 1 mg/mL. Simultaneously, the same protocol was performed with the PS-NPs, without P100 CMF U87-MG, using a 1:1 ratio of PS-NPs and Milli-Q water to compare the results of the subsequent characterization between the bare NPs (PS-NPs) and the G-NPs. Finally, fibroblastcoated nanoparticles (F-NPs) were prepared following the same protocol used for G-NPs, substituting the U87-MG P100 membrane fraction for the P100 fraction isolated from MRC-5 cells.

5.5. Physicochemical Characterization. The physicochemical characterization of both PS-NPs and G-NPs was performed by measuring the hydrodynamic diameter (D_H), surface zeta potential (Z-potential), and polydispersity index (PDI) through dynamic light scattering (DLS) with a Malvern Zetasizer Nano ZS (Malvern Instrument) at a concentration of 20 μ g/mL in Milli-Q water. Additionally, these parameters were evaluated across a pH range of low anionic buffer solutions (pH 4-9) to assess the pH-colloidal stability of both nanosystems. Low anionic buffer solutions were used to reduce the influence of ions on the stability behavior of the colloidal systems. Furthermore, the colloidal stability of both nanosystems was studied by measuring the D_H in different biological media (DMEM supplemented with 10% FBS and 1% PS, serum-free DMEM, and PBS) at 24 and 72 h. All the measurements were performed at a fixed temperature of 25 °C on the Malvern Zetasizer, with light scattering detected at an angle of 173° and taking 3 replicate measurements each time. F-NPs were characterized by measuring their $D_{\rm H}$, PDI, and Z-potential at a concentration of 20 $\mu g/$ mL in Milli-Q water.

In addition, the BC formation of both PS-NPs and G-NPs was investigated. NPs were incubated in supplemented DMEM for 1 h at 37 °C under agitation using a Thermo Shaker (ISTHBLCTS, Ohaus). Subsequently, the soft and hard corona formation was assessed by performing three centrifugations at 20,000xg and 4 °C. Briefly, incubated NPs were centrifuged for the first time and resuspended in low anionic buffer pH 7. This first centrifugation allowed the NPs to be cleared off by biomolecules that had not bound to their surface. Nevertheless, biomolecules that are bound onto NPs remained attached. Therefore, this first centrifugation allowed us to determine soft corona formation. On the other hand, to determine the hard corona formation, NPs were centrifuged and resuspended in low anionic buffer pH 7 two additional times. Lastly, soft and hard BC formation of both PS-NPs and G-NPs was characterized by measuring $D_{\rm H}$, Z-potential, and PDI by DLS along a pH range.

BC formation was also investigated by SDS-PAGE and quantified by a BCA assay. After incubation of NPs with supplemented DMEM and centrifugation at 20000g and 4 °C, the pellets (containing NPs-protein complexes) were collected and labeled as PS-NPs.C and G-NPs.C.). A positive control (total cell lysate of U87-MG) and two

negative controls (bare Ps-NPs and G-NPs not incubated with proteins) were included in the experiment. Subsequently, a mixture of each sample and loading buffer was prepared. Samples were boiled for 3 min for protein denaturation, and 16.8 μ g of each sample (NP concentration) as well as 6 μ L of a molecular weight marker (Thermo Scientific Page-Ruler Plus Prestained Protein Ladder) were loaded into a Bio-Rad 4–20% Mini-PROTEAN® TGXTM Precast Protein Gels. For the running of SDS-PAGE, a constant field of 100 V for 60 min was applied using a PowerPacTM HC High-Current Power Supply and a Mini-PROTEAN Tetra Vertical Electrophoresis Cell (Bio-Rad). Lastly, SDS-Page was revealed with Coomassie Blue. Samples were also characterized for total protein content using the bicinchoninic acid (BCA) assay, following the manufacturer's instructions.

Additionally, proteo-lipid patch membranes (P100) were analyzed for their $D_{\rm H}$, Z-potential, and PDI prior to NP coating. This analysis was conducted to assess the success of the coating process by comparing the differences in size and surface charge between PS-NPs before and after they were wrapped with the P100 membranes to form G-NPs. P100 CMF was sonicated for 3 min before physicochemical characterization, similar to the process employed for the coating. Moreover, the colloidal stability of P100 was also assessed along the pH range.

Ultimately, the CM coating was confirmed by analyzing the morphologies of PS-NPs and G-NPs by high-resolution transmission electron microscopy (HR-TEM, HAADF FEI TITAN G2) operating at 300 kV. TEM imaging samples were prepared by incubating 25 μ L of PS-NPs and G-NPs for 5 min on carbon-coated grids, followed by washing with ultrapure H₂O. Negative staining was performed using uranyl acetate following the standard protocol described in. 61

5.6. Flow Cytometry. The bionanointeractions in vitro between PS-NPs or G-NPs and U87-MG cells were analyzed by flow cytometry (BD AccuriTM C6 Plus Personal Flow Cytometer). U87-MG cells (1.5×10^5) were cultured in 12-well plates, and 24 h later, they were incubated with 20 μ g/mL of the different fluorescent nanosystems for 1, 3, 5, and 24 h. For each time point, three control wells (untreated cells) were included. DMEM was subsequently removed, and cells were detached from each well and washed with PBS. The intensity of FITC was measured by flow cytometry. The measurements of three wells were analyzed as replicates. Additionally, F-NPs and MRC-5 fibroblasts were included to assess the specificity and potential homotypic targeting of the membrane-coated nanoparticles. Bionanointeractions of PS-NPs, G-NPs, and F-NPs with both MRC-5 and U87-MG cells were evaluated using the same flow cytometry protocol and experimental conditions.

5.7. Fluorescence and Confocal Microscopy. PS-NPs or G-NPs and U87-MG cells in vitro bionanointeractions were further investigated using fluorescence and confocal microscopy (Leica DMI 3000 B Manual Inverted Microscope with a K5 sCMOS Microscope Camera, Leica DMI 6000 inverted fluorescence microscope). U87-MG cells (1.5×10^5) were seeded onto tissue culture coverslips and incubated with 20 $\mu g/mL$ of PS-NPs and G-NPs for 1 and 24 h. Afterward, the DMEM was removed, and the coverslips were washed with PBS and fixed with a 4% paraformaldehyde solution (PFA) for 15 min at RT. Subsequently, the samples were subjected to the fluorescent staining protocol. Hoechst-33342 dye (Thermo Scientific Hoechst Solution 33342) was employed to stain the cell nucleus and Alexa Fluor 647 Phalloidin (Invitrogen) was used to label the F-actin of the cell cytoskeleton. The visualization of PS-NPs and G-NPs under fluorescence microscopy was possible due to the employment of commercial NPs loaded with Fluorescein (FITC), as previously detailed. Lastly, the ImageJ Software was used to perform an orthogonal view and a plot Z-axis profile in order to evaluate NP cellular uptake.

5.8. Blood—Brain Barrier Assembly and Transport Study. 5.8.1. Blood—Brain Barrier Assembly and Integrity Characterization. A human BBB in vitro model was assembled to assess the passage of PS-NPs and G-NPs across it. hCMEC/D3 cells were seeded onto polycarbonate membrane on the apical side of a transwell system (Costar Transwell Permeable Supports 12 mm Diameter

Insert 3 μ m Polycarbonate Membrane) as previously described. Before the seeding of hCMEC/D3 cells, each polycarbonate membrane was covered with a thin layer of Rat Collagen I (Cultrex Rat Collagen I lower, Sigma-Aldrich) to better mimic the presence of the in vivo basal lamina. 150 $\mu g/mL$ Rat Collagen I was added to the upper compartment of each well and incubated at 37 °C for 1 h. Then, the upper compartment (apical chamber) was washed 3 times with Milli-Q water and 5×10^4 hCMEC/D3 cells were seeded in 0.5 mL of supplemented EBM-2 medium (LONZA). The lower compartment (basolateral chamber) was filled with 1.5 mL of supplemented EBM-2 medium. Transwell systems were then incubated for 7 days in an atmosphere with 5% CO₂ and 95% humidity at 37 $^{\circ}$ C, changing the supplemented EBM-2 medium at 1, 4, and 7 days. Barrier integrity was assessed at 8 days to ensure that the in vitro BBB model had formed correctly. The transendothelial electrical resistance (TEER) was determined by using automated cellZscope equipment (nanoAnalytics). Once the integrity of the barrier was confirmed, the NP transport studies were performed by adding 20 µg/mL of them in the upper compartment (apical chamber), as detailed in the next paragraph.

5.8.2. PS-NPs and G-NPs Transport Study across the In Vitro BBB Model. The transported mass percentage of PS-NPs and G-NPs was determined across the in vitro BBB model. The passage of PS-NPs and G-NPs through the BBB model (hCMEC/D3 monolayer) was evaluated at day 8 at different experimental time points (1, 3, and 5 h). As a control experiment, the passage of PS-NPs and G-NPs across an empty polycarbonate monolayer (without hCMEC/D3 monolayer) was also evaluated. Specifically, PS-NPs and G-NPs were diluted in supplemented EBM-2 medium at a concentration of 20 μ g/ mL and added to the upper compartment (apical chamber). 1.5 mL portion of supplemented EBM-2 medium was also added to the lower compartment (basolateral chamber) of each well. After 1, 3, and 5 h, 100 µL from the basolateral chamber was removed and stored for later fluorescence analysis. At the same time, 100 μ L of fresh medium was added to the basolateral chamber to maintain the apical/ basolateral volume ratio. The entire experiment was carried out under restiveness using an ES-20 Orbital Shaker-Incubator at 37 °C and 50 rpm (Biosan, LVA). Lastly, PS-NPs and G-NPs fluorescence from the basolateral chamber sampling was determined using a UV-vis-NIR HORIBA QuantaMaster-8000 (QM-8000) (Horiba, JPN) with an excitation/emission wavelength of 505/515 nm. The final transported mass percentage of PS-NPs and G-NPs through the in vitro BBB model was determined by evaluating the concentration of PS-NPs or G-NPs in the basolateral chamber at each experimental time. Serial dilutions of PS-NPs and G-NPs in the range of 0-3.91 μ g/mL in EBM-2 were prepared to obtain a calibration curve. Linear regression was applied to define the correlation between the fluorescence intensity and PS-NPs and G-NPs mass concentration and used to determine the total mass of PS-NPs and G-NPs in the basolateral chamber. The apparent permeability $(P_{\rm app})$ was then determined using the equation:

$$P_{\rm app} = \frac{1}{A} C_0 \frac{\mathrm{d}Q}{\mathrm{d}t}$$

where A represents the surface area of the membrane in cm², C_0 is the initial concentration of PS-NPs and G-NPs in the apical compartment $(\mu g/mL)$, and dQ/dt is the amount of PS-NPs and G-NPs that appears in the basolateral compartment in the given time period $(\mu g/min)$. For every time point, 9 wells were designated for each experimental condition (3 controls to evaluate the passage of PS-NPs and G-NPs without barrier and 9 wells to assess the passage of PS-NPs and G-NPs through the cell barrier). This way, the measurements of 9 wells were analyzed as replicates.

Furthermore, the barrier integrity was measured by TEER after 5 h of PS-NPs and G-NPs exposure.

5.9. Statistical Analysis. The results are presented as the mean of at least 3 different replicates with either standard deviation or standard error, unless otherwise stated. All statistical analyses were performed by IBM SPSS Statistics and Origin software for graph generation.

ASSOCIATED CONTENT

5 Supporting Information

The Supporting Information is available free of charge at https://pubs.acs.org/doi/10.1021/acsami.5c07306.

Schematic representation of the cell membrane (CM) protocols tested; protein content of P17 and P100 fractions following the different CM isolation protocols; original SDS-PAGE and Western blotting; colloid stability table and graph; table with soft and hard corona analysis by DLS; SDS-PAGE of protein corona and protein quantification by BCA assay; fluorescence microscopy images of U87-MG cells exposed to PS-NPs and G-NPs; bionanointeractions of cell membranecoated nanoparticles with fibroblasts and glioblastoma cells analyzed by flow cytometry; Z-axis fluorescence analysis at 24 h exposure of PS-NPs and G-NPs with U87-MG cells in confocal microscopy images; TEER of the in vitro BBB model before and after nanoparticle exposure; and transported mass of nanoparticles across the in vitro BBB model (PDF)

AUTHOR INFORMATION

Corresponding Authors

Paola Sánchez-Moreno — Department of Applied Physics, Faculty of Sciences, Universidad de Granada, 18071 Granada, Spain; orcid.org/0000-0002-9560-4629; Email: paolasm@ugr.es

Mattia Bramini — Department of Cell Biology, Faculty of Sciences, Universidad de Granada, 18071 Granada, Spain; oocid.org/0000-0002-0381-9391; Email: mbramini@ugr.es

Authors

Daniel Jiménez-Boland — Department of Cell Biology, Faculty of Sciences and Department of Applied Physics, Faculty of Sciences, Universidad de Granada, 18071 Granada, Spain; orcid.org/0009-0000-9284-4902

Ana Robles-Fernández — Department of Cell Biology, Faculty of Sciences and Department of Applied Physics, Faculty of Sciences, Universidad de Granada, 18071 Granada, Spain; orcid.org/0009-0006-8274-4557

Antonio Martín-Rodríguez – Department of Applied Physics, Faculty of Sciences, Universidad de Granada, 18071 Granada, Spain; orcid.org/0000-0001-7161-5086

Miguel Angel Cuadros – Department of Cell Biology, Faculty of Sciences, Universidad de Granada, 18071 Granada, Spain José Angel Traverso – Department of Cell Biology, Faculty of Sciences, Universidad de Granada, 18071 Granada, Spain

Complete contact information is available at: https://pubs.acs.org/10.1021/acsami.5c07306

Author Contributions

§D.J.-B. and A.R.-F. contributed equally to this work; co-first authors.

Author Contributions

 $^{\parallel}\text{P.S.-M.}$ and M.B. contributed equally to this work; co-last authors.

Notes

The authors declare no competing financial interest.

ACKNOWLEDGMENTS

The authors gratefully acknowledge the funding provided by Grant PID2021-12436OA-I00 funded by MICIU/AEI/10.13039/501100011033 and by ERDF, EU. D. Jiménez Boland and A. Robles-Fernández wish to thank MICIN for their respective Ph.D. student fellowships (FPU22/01773 and PRE2022-103642, respectively). M. Bramini extends appreciation for support under the Ramón y Cajal program, MCIN/AEI (RYC2019-027692-I). Finally, the authors express their gratitude to the Scientific Instrumentation Centre (CIC) at the University of Granada for their valuable technical assistance.

REFERENCES

- (1) Zong, H.; Parada, L. F.; Baker, S. J. Cell of Origin for Malignant Gliomas and Its Implication in Therapeutic Development. *Cold Spring Harb Perspect Biol.* **2015**, *7* (5), No. a020610.
- (2) Wan, S.; Zhang, G.; Liu, R.; Abbas, M. N.; Cui, H. Pyroptosis, Ferroptosis, and Autophagy Cross-Talk in Glioblastoma Opens up New Avenues for Glioblastoma Treatment. *Cell Communication and Signaling* **2023**, *21* (1), 115.
- (3) Patel, V.; Chavda, V. Intraoperative Glioblastoma Surgery-Current Challenges and Clinical Trials: An Update. *Cancer Pathogenesis and Therapy* **2024**, 2, 256.
- (4) Cruz, J. V. R.; Batista, C.; Afonso, B. de H.; Alexandre-Moreira, M. S.; Dubois, L. G.; Pontes, B.; Moura Neto, V.; Mendes, F. de A. Obstacles to Glioblastoma Treatment Two Decades after Temozolomide. *Cancers* **2022**, *14* (13), 3203.
- (5) Stepanenko, A. A.; Chekhonin, V. P. On the Critical Issues in Temozolomide Research in Glioblastoma: Clinically Relevant Concentrations and MGMT-Independent Resistance. *Biomedicines* **2019**, 7 (4), 92.
- (6) Narsinh, K. H.; Perez, E.; Haddad, A. F.; Young, J. S.; Savastano, L.; Villanueva-Meyer, J. E.; Winkler, E.; de Groot, J. Strategies to Improve Drug Delivery Across the Blood–Brain Barrier for Glioblastoma. *Curr. Neurol Neurosci Rep* **2024**, *24* (5), 123–139.
- (7) Di Mascolo, D.; Guerriero, I.; Pesce, C.; Spanò, R.; Palange, A. L.; Decuzzi, P. μ MESH-Enabled Sustained Delivery of Molecular and Nanoformulated Drugs for Glioblastoma Treatment. *ACS Nano* **2023**, 17 (15), 14572–14585.
- (8) Castagnola, V.; Deleye, L.; Podestà, A.; Jaho, E.; Loiacono, F.; Debellis, D.; Trevisani, M.; Ciobanu, D. Z.; Armirotti, A.; Pisani, F.; Flahaut, E.; Vazquez, E.; Bramini, M.; Cesca, F.; Benfenati, F. Interactions of Graphene Oxide and Few-Layer Graphene with the Blood—Brain Barrier. *Nano Lett.* **2023**, 23 (7), 2981–2990.
- (9) Bramini, M.; Ye, D.; Hallerbach, A.; Nic Raghnaill, M.; Salvati, A.; Åberg, C.; Dawson, K. A. Imaging Approach to Mechanistic Study of Nanoparticle Interactions with the Blood—Brain Barrier. *ACS Nano* **2014**, 8 (5), 4304–4312.
- (10) Shabani, L.; Abbasi, M.; Azarnew, Z.; Amani, A. M.; Vaez, A. Neuro-Nanotechnology: Diagnostic and Therapeutic Nano-Based Strategies in Applied Neuroscience. *BioMed. Eng. OnLine* **2023**, 22 (1), 1.
- (11) Schuster, T.; Mühlstein, A.; Yaghootfam, C.; Maksimenko, O.; Shipulo, E.; Gelperina, S.; Kreuter, J.; Gieselmann, V.; Matzner, U. Potential of Surfactant-Coated Nanoparticles to Improve Brain Delivery of Arylsulfatase A. J. Controlled Release 2017, 253, 1–10.
- (12) Tosi, G.; Duskey, J. T.; Kreuter, J. Nanoparticles as Carriers for Drug Delivery of Macromolecules across the Blood-Brain Barrier. *Expert Opin Drug Deliv* **2020**, *17* (1), 23–32.
- (13) Song, X.; Qian, H.; Yu, Y. Nanoparticles Mediated the Diagnosis and Therapy of Glioblastoma: Bypass or Cross the Blood-Brain Barrier. *Small* **2023**, *19* (45), No. 2302613.
- (14) Zhang, Z.; Guan, J.; Jiang, Z.; Yang, Y.; Liu, J.; Hua, W.; Mao, Y.; Li, C.; Lu, W.; Qian, J.; Zhan, C. Brain-Targeted Drug Delivery by Manipulating Protein Corona Functions. *Nat. Commun.* **2019**, *10*, 3561.

- (15) Heggannavar, G. B.; Vijeth, S.; Kariduraganavar, M. Y. Preparation of Transferrin-Conjugated Poly- ε -Caprolactone Nanoparticles and Delivery of Paclitaxel to Treat Glioblastoma across Blood–Brain Barrier. *emergent mater.* **2019**, 2 (4), 463–474.
- (16) Ramalho, M. J.; Bravo, M.; Loureiro, J. A.; Lima, J.; Pereira, M. C. Transferrin-Modified Nanoparticles for Targeted Delivery of Asiatic Acid to Glioblastoma Cells. *Life Sciences* **2022**, 296, No. 120435.
- (17) Wagner, S.; Zensi, A.; Wien, S. L.; Tschickardt, S. E.; Maier, W.; Vogel, T.; Worek, F.; Pietrzik, C. U.; Kreuter, J.; von Briesen, H. Uptake Mechanism of ApoE-Modified Nanoparticles on Brain Capillary Endothelial Cells as a Blood-Brain Barrier Model. *PLoS One* **2012**, *7* (3), No. e32568.
- (18) Bashiri, G.; Padilla, M. S.; Swingle, K. L.; Shepherd, S. J.; Mitchell, M. J.; Wang, K. Nanoparticle Protein Corona: From Structure and Function to Therapeutic Targeting. *Lab Chip* **2023**, 23 (6), 1432–1466.
- (19) Fang, R. H.; Hu, C.-M. J.; Luk, B. T.; Gao, W.; Copp, J. A.; Tai, Y.; O'Connor, D. E.; Zhang, L. Cancer Cell Membrane-Coated Nanoparticles for Anticancer Vaccination and Drug Delivery. *Nano Lett.* **2014**, *14* (4), 2181–2188.
- (20) Liu, H.; Su, Y.-Y.; Jiang, X.-C.; Gao, J.-Q. Cell Membrane-Coated Nanoparticles: A Novel Multifunctional Biomimetic Drug Delivery System. *Drug Delivery and Transl. Res.* **2023**, *13* (3), 716–737.
- (21) Li, J.; Wei, Y.; Zhang, C.; Bi, R.; Qiu, Y.; Li, Y.; Hu, B. Cell-Membrane-Coated Nanoparticles for Targeted Drug Delivery to the Brain for the Treatment of Neurological Diseases. *Pharmaceutics* **2023**, *15* (2), 621.
- (22) Shi, P.; Xu, J.; Cui, H. The Recent Research Progress of NF-κB Signaling on the Proliferation, Migration, Invasion, Immune Escape and Drug Resistance of Glioblastoma. *International Journal of Molecular Sciences* **2023**, 24 (12), 10337.
- (23) Otręba, M.; Stojko, J.; Kabała-Dzik, A.; Rzepecka-Stojko, A. Perphenazine and Prochlorperazine Decrease Glioblastoma U-87 MG Cell Migration and Invasion: Analysis of the ABCB1 and ABCG2 Transporters, E-Cadherin, α -Tubulin and Integrins (A3, A5, and B1) Levels. *Oncology Letters* **2022**, 23 (6), 182.
- (24) Chi, S.; Zhang, L.; Cheng, H.; Chang, Y.; Zhao, Y.; Wang, X.; Liu, Z. Biomimetic Nanocomposites Camouflaged with Hybrid Cell Membranes for Accurate Therapy of Early-Stage Glioma. *Angew. Chem. Int. Ed* **2023**, 62 (29), No. e202304419.
- (25) De Pasquale, D.; Marino, A.; Tapeinos, C.; Pucci, C.; Rocchiccioli, S.; Michelucci, E.; Finamore, F.; McDonnell, L.; Scarpellini, A.; Lauciello, S.; Prato, M.; Larrañaga, A.; Drago, F.; Ciofani, G. Homotypic Targeting and Drug Delivery in Glioblastoma Cells through Cell Membrane-Coated Boron Nitride Nanotubes. *Materials & Design* **2020**, *192*, No. 108742.
- (26) Zou, Y.; Wang, Y.; Xu, S.; Liu, Y.; Yin, J.; Lovejoy, D. B.; Zheng, M.; Liang, X.; Park, J. B.; Efremov, Y. M.; Ulasov, I.; Shi, B. Brain Co-Delivery of Temozolomide and Cisplatin for Combinatorial Glioblastoma Chemotherapy. *Adv. Mater.* **2022**, *34* (33), No. 2203958.
- (27) Huang, X.; Mu, N.; Ding, Y.; Huang, R.; Wu, W.; Li, L.; Chen, T. Tumor Microenvironment Targeting for Glioblastoma Multiforme Treatment via Hybrid Cell Membrane Coating Supramolecular Micelles. J. Controlled Release 2024, 366, 194–203.
- (28) Liu, L.; Bai, X.; Martikainen, M.-V.; Kårlund, A.; Roponen, M.; Xu, W.; Hu, G.; Tasciotti, E.; Lehto, V.-P. Cell Membrane Coating Integrity Affects the Internalization Mechanism of Biomimetic Nanoparticles. *Nat. Commun.* **2021**, *12* (1), 5726.
- (29) Johnson, D. T.; Zhou, J.; Kroll, A. V.; Fang, R. H.; Yan, M.; Xiao, C.; Chen, X.; Kline, J.; Zhang, L.; Zhang, D.-E. Acute Myeloid Leukemia Cell Membrane-Coated Nanoparticles for Cancer Vaccination Immunotherapy. *Leukemia* **2022**, *36* (4), 994–1005.
- (30) Molina-Bolívar, J. A.; Ortega-Vinuesa, J. L. How Proteins Stabilize Colloidal Particles by Means of Hydration Forces. *Langmuir* **1999**, *15* (8), 2644–2653.

- (31) Baimanov, D.; Wang, J.; Zhang, J.; Liu, K.; Cong, Y.; Shi, X.; Zhang, X.; Li, Y.; Li, X.; Qiao, R.; Zhao, Y.; Zhou, Y.; Wang, L.; Chen, C. In Situ Analysis of Nanoparticle Soft Corona and Dynamic Evolution. *Nat. Commun.* **2022**, *13* (1), 5389.
- (32) Graván, P.; Peña-Martín, J.; de Andrés, J. L.; Pedrosa, M.; Villegas-Montoya, M.; Galisteo-González, F.; Marchal, J. A.; Sánchez-Moreno, P. Exploring the Impact of Nanoparticle Stealth Coatings in Cancer Models: From PEGylation to Cell Membrane-Coating Nanotechnology. ACS Appl. Mater. Interfaces 2024, 16 (2), 2058—2074.
- (33) Docter, D.; Distler, U.; Storck, W.; Kuharev, J.; Wünsch, D.; Hahlbrock, A.; Knauer, S. K.; Tenzer, S.; Stauber, R. H. Quantitative Profiling of the Protein Coronas That Form around Nanoparticles. *Nat. Protoc* **2014**, *9* (9), 2030–2044.
- (34) Lamson, N. G.; Pickering, A. J.; Wyckoff, J.; Ganesh, P.; Calle, E. A.; Straehla, J. P.; Hammond, P. T. Trafficking through the Blood—Brain Barrier Is Directed by Core and Outer Surface Components of Layer-by-Layer Nanoparticles. *Bioengineering & Translational Medicine* 2024, 9 (4), No. e10636.
- (35) Jin, F.; Qi, J.; Liu, D.; You, Y.; Shu, G.; Du, Y.; Wang, J.; Xu, X.; Ying, X.; Ji, J.; Du, Y. Cancer-Cell-Biomimetic Upconversion Nanoparticles Combining Chemo-Photodynamic Therapy and CD73 Blockade for Metastatic Triple-Negative Breast Cancer. *J. Controlled Release* **2021**, 337, 90–104.
- (36) Zhong, Z.; Deng, W.; Wu, J.; Shang, H.; Tong, Y.; He, Y.; Huang, Q.; Ba, X.; Chen, Z.; Tang, K. Cell Membrane Coated Nanoparticles as a Biomimetic Drug Delivery Platform for Enhancing Cancer Immunotherapy. *Nanoscale* **2024**, *16* (18), 8708–8738.
- (37) Fernández-Borbolla, A.; García-Hevia, L.; Fanarraga, M. L. Cell Membrane-Coated Nanoparticles for Precision Medicine: A Comprehensive Review of Coating Techniques for Tissue-Specific Therapeutics. *International Journal of Molecular Sciences* **2024**, 25 (4), 2071.
- (38) Zhang, Q.; Dehaini, D.; Zhang, Y.; Zhou, J.; Chen, X.; Zhang, L.; Fang, R. H.; Gao, W.; Zhang, L. Neutrophil Membrane-Coated Nanoparticles Inhibit Synovial Inflammation and Alleviate Joint Damage in Inflammatory Arthritis. *Nat. Nanotechnol.* **2018**, *13* (12), 1182–1190.
- (39) Parodi, A.; Quattrocchi, N.; Van De Ven, A. L.; Chiappini, C.; Evangelopoulos, M.; Martinez, J. O.; Brown, B. S.; Khaled, S. Z.; Yazdi, I. K.; Enzo, M. V.; Isenhart, L.; Ferrari, M.; Tasciotti, E. Synthetic Nanoparticles Functionalized with Biomimetic Leukocyte Membranes Possess Cell-like Functions. *Nat. Nanotechnol.* **2013**, 8 (1), 61–68.
- (40) Chen, H.-Y.; Deng, J.; Wang, Y.; Wu, C.-Q.; Li, X.; Dai, H.-W. Hybrid Cell Membrane-Coated Nanoparticles: A Multifunctional Biomimetic Platform for Cancer Diagnosis and Therapy. *Acta Biomaterialia* **2020**, *112*, 1–13.
- (41) Xia, Q.; Zhang, Y.; Li, Z.; Hou, X.; Feng, N. Red Blood Cell Membrane-Camouflaged Nanoparticles: A Novel Drug Delivery System for Antitumor Application. *Acta Pharm. Sin B* **2019**, 9 (4), 675–689.
- (42) Radoń, A.; Włodarczyk, A.; Sieroń, Ł.; Rost-Roszkowska, M.; Chajec, Ł.; Łukowiec, D.; Ciuraszkiewicz, A.; Gębara, P.; Wacławek, S.; Kolano-Burian, A. Influence of the Modifiers in Polyol Method on Magnetically Induced Hyperthermia and Biocompatibility of Ultrafine Magnetite Nanoparticles. *Sci. Rep* **2023**, *13* (1), 7860.
- (43) Fröhlich, E. The Role of Surface Charge in Cellular Uptake and Cytotoxicity of Medical Nanoparticles. *IJN* **2012**, *7*, 5577–5591.
- (44) Surapaneni, S. K.; Bashir, S.; Tikoo, K. Gold Nanoparticles-Induced Cytotoxicity in Triple Negative Breast Cancer Involves Different Epigenetic Alterations Depending upon the Surface Charge. *Sci. Rep* **2018**, *8* (1), 12295.
- (45) Miao, Y.-B.; Zhao, W.; Renchi, G.; Gong, Y.; Shi, Y. Customizing Delivery Nano-Vehicles for Precise Brain Tumor Therapy. *J. Nanobiotechnology* **2023**, *21* (1), 32.
- (46) Zhao, T.; Ren, M.; Shi, J.; Wang, H.; Bai, J.; Du, W.; Xiang, B. Engineering the Protein Corona: Strategies, Effects, and Future

- Directions in Nanoparticle Therapeutics. Biomedicine & Pharmacotherapy 2024, 175, No. 116627.
- (47) Schvartz, M.; Saudrais, F.; Devineau, S.; Chédin, S.; Jamme, F.; Leroy, J.; Rakotozandriny, K.; Taché, O.; Brotons, G.; Pin, S.; Boulard, Y.; Renault, J.-P. Role of the Protein Corona in the Colloidal Behavior of Microplastics. *Langmuir* **2023**, *39* (12), 4291–4303.
- (48) Huang, Y.; Zhang, B.; Xie, S.; Yang, B.; Xu, Q.; Tan, J. Superparamagnetic Iron Oxide Nanoparticles Modified with Tween 80 Pass through the Intact Blood-Brain Barrier in Rats under Magnetic Field. ACS Appl. Mater. Interfaces 2016, 8 (18), 11336—11341.
- (49) White, J.; White, M. P. J.; Wickremesekera, A.; Peng, L.; Gray, C. The Tumour Microenvironment, Treatment Resistance and Recurrence in Glioblastoma. *Journal of Translational Medicine* **2024**, 22 (1), 540.
- (50) Olivier, C.; Oliver, L.; Lalier, L.; Vallette, F. M. Drug Resistance in Glioblastoma: The Two Faces of Oxidative Stress. *Front. Mol. Biosci.* **2021**, *7*, No. 620677.
- (51) Blanchard, R.; Adjei, I. Engineering the Glioblastoma Microenvironment with Bioactive Nanoparticles for Effective Immunotherapy. RSC Adv. 2023, 13 (45), 31411–31425.
- (52) Graván, P.; Peña-Martín, J.; Andrés, J. L.; Pedrosa, M.; Villegas-Montoya, M.; Galisteo-González, F.; Marchal, J. A.; Sánchez-Moreno, P. Exploring the Impact of Nanoparticle Stealth Coatings in Cancer Models: From PEGylation to Cell Membrane-Coating Nanotechnology. ACS Appl. Mater. Interfaces 2024, 16, 2058–2074.
- (53) Zeng, S.; Tang, Q.; Xiao, M.; Tong, X.; Yang, T.; Yin, D.; Lei, L.; Li, S. Cell Membrane-Coated Nanomaterials for Cancer Therapy. *Materials Today Bio* **2023**, *20*, No. 100633.
- (54) Li, L.; Yang, Y.; Wang, L.; Xu, F.; Li, Y.; He, X. The Effects of Serum Albumin Pre-Adsorption of Nanoparticles on Protein Corona and Membrane Interaction: A Molecular Simulation Study. *J. Mol. Biol.* **2023**, 435 (1), No. 167771.
- (55) Jin, J.; Bhujwalla, Z. M. Biomimetic Nanoparticles Camouflaged in Cancer Cell Membranes and Their Applications in Cancer Theranostics. *Frontiers in Oncology* **2020**, *9*, 2019.
- (56) Ghaznavi, H.; Afzalipour, R.; Khoei, S.; Sargazi, S.; Shirvalilou, S.; Sheervalilou, R. New Insights into Targeted Therapy of Glioblastoma Using Smart Nanoparticles. *Cancer Cell Int.* **2024**, 24 (1), 160.
- (57) Zhang, J.; Li, T.; Liu, L.; Chen, Z.; Li, L.; Yao, X.; Cheng, J.; Hu, X.; Guo, J.; Li, R.; Ge, C.; Ling, E.-A.; Yao, H. A Novel PH1/pE27HGFK1 Nanoparticles for Orthotopic Glioblastoma Therapy. *Cancer Nanotechnol.* **2024**, *15* (1), 29.
- (58) Chen, H.; Ji, J.; Zhang, L.; Luo, C.; Chen, T.; Zhang, Y.; Ma, C.; Ke, Y.; Wang, J. Nanoparticles Coated with Brain Microvascular Endothelial Cell Membranes Can Target and Cross the Blood–Brain Barrier to Deliver Drugs to Brain Tumors. *Small* **2024**, 20 (29), No. 2306714.
- (59) Han, S.; Lee, Y.; Lee, M. Biomimetic Cell Membrane-Coated DNA Nanoparticles for Gene Delivery to Glioblastoma. *J. Controlled Release* **2021**, 338, 22–32.
- (60) Kim, J.-K.; Uchiyama, S.; Gong, H.; Stream, A.; Zhang, L.; Nizet, V. Engineered Biomimetic Platelet Membrane-Coated Nanoparticles Block Staphylococcus Aureus Cytotoxicity and Protect Against Lethal Systemic Infection. *Engineering* **2021**, 7 (8), 1149–1156.
- (61) Sui, B.; Zhao, J.; Ding, T.; Ruan, M.; Sun, J.; Liu, X. Cell Membrane Camouflaged Mesoporous Bioactive Glass Nanoparticles Embedding Glucose Oxidase for Enhancing Targeted Anti-Tumor Catalytic Therapy. *Applied Materials Today* **2023**, 32, No. 101813.